Astronomy & Astrophysics manuscript no. aa
September 17, 2013

Quiescent thermal emission from neutron stars in LMXBs

A. Turlione[1], D.N. Aguilera[1,2] and J. A. Pons[3]

[1] Laboratorio Tandar, CNEA-CONICET, Av. Gral Paz 1499, 1430 San Martín, Buenos Aires, Argentina

[2] Deutsches Zentrum für Luft-und Raumfahrt, DLR-RY, Robert-Hooke Str. 7, 28359 Bremen, Germany

[3] Departament de Física Aplicada, Universitat d'Alacant, Ap. Correus 99, 03080 Alacant, Spain

ABSTRACT

Context. The quiescent thermal emission from neutron stars in low mass X-ray binaries after active periods of intense activity in x-rays (outbursts) has been monitored.
Aims. The theoretical modeling of the thermal relaxation of the neutron star crust may be used to establish constraints on the crust and envelope composition and transport properties, depending on the astrophysical scenarios assumed.
Methods. We perform numerical simulations of the neutron star crust thermal evolution and compare them with inferred surface temperatures for five sources: MXB 1659−29, KS 1731−260, XTE J1701−462, EXO 0748−676 and IGR J17480−2446. We also present stationary envelope models to be used as a boundary condition for the crustal cooling models.
Results. We obtain a relation between the mass accretion rate and the temperature reached at the crust-envelope interface at the end of the active phase that accounts for early observations and reduces the number of free parameters of the problem. With this relation we are also able to set constraints to the envelope composition depending on the accretion mass rate. We find that the evolution of MXB 1659−29, KS 1731−260 and EXO 0748−676 can be well described within a deep crustal cooling scenario. Conversely, we find that other two sources can only be explained with models beyond crustal cooling. For the peculiar emission of XTE J1701−462 we propose alternative scenarios like residual accretion during quiescence, additional heat sources in the outer crust and/or thermal isolation of the inner crust due to a buried magnetic field. We also explain the very recent reported temperature of IGR J17480−2446 with an extra heat deposition in the outer crust coming from shallow sources.

Key words. stars: neutron, X-rays: binaries

1. Introduction

Low-mass X-ray binaries (LMXBs) are systems formed by a neutron star (NS) or a black hole that accretes matter from a low-mass companion star. These systems are most of the time in a quiescent state where little accretion occurs with an X-ray luminosity $< 10^{34}\,\mathrm{erg\,s^{-1}}$. Periodically, the compact object undergoes an accretion episode with the corresponding increase in luminosity $\sim 10^{36}$-$10^{39}\,\mathrm{erg\,s^{-1}}$. The accreted hydrogen and helium-rich material at rates $\sim 10^{15}$–$10^{18}\,\mathrm{g\,s^{-1}}$ undergoes thermonuclear fusion within hours to days of reaching the NS surface, releasing ≈ 5 MeV/nucleon (see e.g. Bildsten (1997); Schatz et al. (1999) for seminal work). The nuclear burning is thermally unstable on weakly magnetized NSs ($B \ll 10^{11}$ G) accreting at $\dot{M} < 10^{18}\,\mathrm{g\,s^{-1}}$ and produces energetic (10^{39} erg) type I X-ray bursts when $\dot{M} < 10^{17}\,\mathrm{g\,s^{-1}}$. For steady state models at higher accretion rates, the flux is dominated by the nuclear energy released from the conversion of hydrogen and helium to heavy elements.

At the end of an active period, the emission shows a decreasing X-ray activity (quiescent phase) until a new accretion cycle begins. Most of the sources accrete for days or weeks but there are only few of them that show unusually long active phases that last for years or decades. Recently, five so-called *quasi-persistent* sources have been monitored for about 10^3 days after the end of the outburst: MXB 1659−29 (Wijnands et al. (2003); Cackett et al. (2008)), KS 1731−260 (Wijnands et al. (2001); Cackett et al. (2010a)), EXO 0748−676 (Wolff et al. (2008); Degenaar et al. (2011b); Díaz Trigo et al. (2011)), XTE J1701−462 (Fridriksson et al. (2010, 2011)) and IGR J17480−2446 (Degenaar & Wijnands (2011a)). All these sources have been accreting at rates $\simeq$ 0.01–1 times the Eddington mass accretion rate, $\dot{M} \simeq 10^{18}\,\mathrm{g\,s^{-1}}$(Galloway et al. (2008); Degenaar et al. (2011b)). The thermal component of the spectra is consistent with an overall decrease in the surface temperature of the NS; only for one source, MXB 1659−29, last measurements indicate that the star has reached an equilibrium temperature[1] but for the others there is evidence for continued cooling (Fridriksson et al. (2011)).

Theoretical explanations of the origin of the quiescent X-ray emission point to the thermal relaxation of the crust. Before the active phase it is assumed that the NS is old enough to have an isothermal interior and its surface temperature reflects the core temperature. During outbursts, the crust is heated up beyond thermal equilibrium due to the accretion of matter that compresses the crust and triggers nuclear reactions. Once accretion falls to quiescent lev-

[1] While this work was being written, a new observation of MXB 1659−29 was reported which temperature has not been clearly determined yet (see discussion in Cackett et al. (2013)); we are not taking it into account in our analysis.

els, it cools down by thermal radiation (mainly in the X-ray band) as the outer layers return to equilibrium with the interior; see pioneering work done by Brown et al. (1998) and Colpi et al. (2001). In quasi-persistent sources the crust is the region that is heated up because the outburst duration ($\sim$ yrs) is of the same order than the crustal diffusion timescale; in ordinary sources accreting for much shorter time the heat is generated mostly by thermonuclear reactions in the envelope diffusing rapidly ($\sim$ s,min) and without affecting the interior thermal state.

As a result of this long-term accretion phase, the cooling is modified not only by the energy released in the envelope (at densities 10^4–$10^7 \mathrm{g\,cm^{-3}}$) due to thermonuclear reactions, but also by the energy generated in the inner crust (at 10^{11}–$10^{13} \mathrm{g\,cm^{-3}}$) due to electron captures, neutron emission, and density-driven nuclear fusion reactions (pycnonuclear reactions). Crustal heating is mostly supplied by pycnonuclear reactions in the inner crust but their rates have huge uncertainties: what particular reaction is taking place and at which density is still unknown. Fortunately, this uncertainty does not significantly affect the value of the total heat released $Q_{\rm tot} \simeq 1.9$ MeV (Haensel & Zdunik (2008) hereafter HZ08, Gupta et al. (2007)), although the spatial distribution of heat sources in the inner crust is uncertain.

In the last decade the comparison of observational data with cooling models including deep crustal heating allowed to investigate crust properties and ultra-dense matter processes with influence on the cooling curves (Rutledge et al. 2002). Simulations of the crust relaxation after bursts for KS 1731−260 and MXB 1659−29 (Shternin et al. (2007) and Brown & Cumming (2009); hereafter Sh07 and BC09, respectively) suggested a rather high thermal conductivity in the outer crust (which requires a low impurity content) in agreement with recent molecular dynamics calculations (Horowitz et al. 2009) but in controversy with the inefficient crust conductivity necessary for carbon ignition in super-bursts (Cooper & Narayan 2005; Cumming et al. 2006).

Many other open issues as well as new observational data pose challenges to these models in several fronts. First some of the sources could be still cooling, as indicated by the last observation of KS 1731−260 (Fridriksson et al. 2011) and high temperatures exhibit in XTE J1701−462. If these sources indeed continue cooling, models should account for longer relaxation times for the crust. This opens the possibility to revisit the analysis done in BC09 who assumed that the quiescent emission of the crust levels off with the core. Second, the variability of some sources in the thermal component: XTE J1701−462 has shown relatively short periods of increased temperatures during an overall cooling evolution. The origin of this variation is not clear and one possible explanation is low level accretion onto the NS surface during quiescence due to the correlated variability observed in the power-law spectral component (Fridriksson et al. 2011). Third, one more candidate for crustal cooling has been recently detected in the globurar cluster Terzan 5, IGR J17480−2446, which exhibits a large temperature in comparison with the quiescent base level in 2009 (Degenaar et al. 2011b). BC09-type cooling models could only account temperatures inferred at two events if there is an extra heat generation in the outer crust (Degenaar et al. 2011a) whose location and origin is unknown[2]. Moreover, very recently new five IGR J17480−2446 observations have been reported (Degenaar et al. 2013) making its overall cooling even more puzzling.

In this paper, we aim at revisiting the problem by performing time-dependent simulations of the thermal evolution of the NS crust with deep crustal heating, starting from previously calculated stationary solutions for the envelope using the same underlying NS model. In this way we treat the envelope and the crust in a consistent way. As a step further, we obtain a functional relation between the mass accretion rate during outburst and the temperature at the base of the envelope at the beginning of the quiescence phase, thus, reducing the number of free parameters. The main purpose is to use our models to constrain general properties of the crust and envelope (e.g. envelope composition, impurities in the crust, etc.) by comparing to observational data of all available sources. We also discuss alternative scenarios that explain some peculiarities in the emission of the two objects (EXO 0748−676 and XTE J1701−462) that fall beyond the canonical model.

The paper is organized as follows: in Sec. 2 we present a description of the five sources KS 1731−260, MXB 1659−29, EXO 0748−676, XTE J1701−462, and IGR J17480−2446, and compare their remarkable characteristics. In Sec. 3, we describe the microphysics of the underlying neutron star model used in the simulations. The thermal evolution and the details for the numerical code are presented in Sec. 4 while in Sec. 5 we present stationary envelope models and a relation between the mass accretion rate and the temperature at the base of the envelope. In the subsequent Secs. 6-10.3 we test in detail our cooling simulations within and beyond the crustal cooling for the four sources. Finally we summarize general conclusions in Sec. 11.

2. Sources

We now discuss the main observational facts of the five NSs in LMXBs detected in quiescence, summarized in Fig. 1 and Tab. 1.

2.1. MXB 1659−29

This source was detected in outburst first in 1976-1979 and again in 1999-2001. Both outbursts lasted about 2.5 years (Lewin et al. 1976). Its quiescence was monitored by *Chandra* and *XMM-Newton* telescopes, being the last observation made by *Chandra* 11 years after the end of the last outburst (Fig. 1a). Assuming an accretion power luminosity $L = \epsilon \dot{M} c$, with $\epsilon = 0.2$, it is possible to estimate a mean value for the mass accretion rate $\dot{M}_{\rm obs,18} \simeq 0.07 - 0.18$, where $\dot{M}_{\rm obs,18}$ is in units of $10^{18}\,\mathrm{g\,s^{-1}}$, (Galloway et al. 2008).

The first six observations of this source can be interpreted as the crust cooling down to equilibrium with the core. The evolution of the surface temperature can be fitted with an exponential function $T(t) = ae^{-(t-t_0)/\tau+b}$ with

[2] Another NSs went on quiescence in Terzan 5, EXO 1745−248 (Degenaar & Wijnands 2012), but it cannot be consider for crustal cooling since it lacks from thermal emission; nevertheless it sets strong constraints on the properties on the NS core, which has efficiently cooled off.

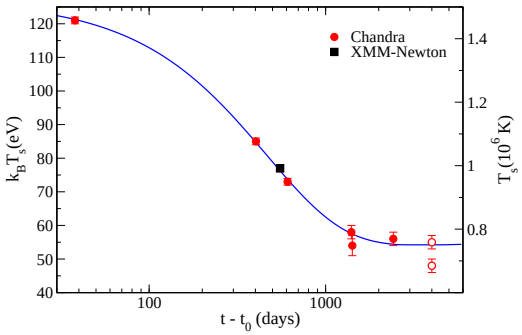

(a) **MXB 1659−29**, data and fits from Cackett et al. (2008) and Cackett et al. (2013) (open symbols).

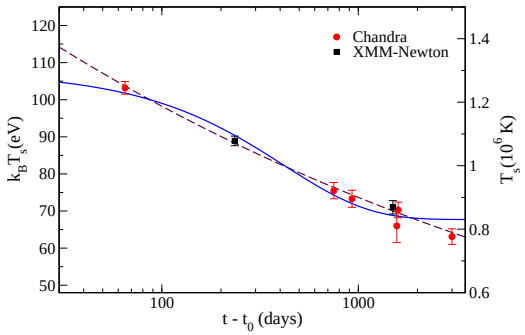

(b) **KS 1731−260**, data and fits from Cackett et al. (2010a).

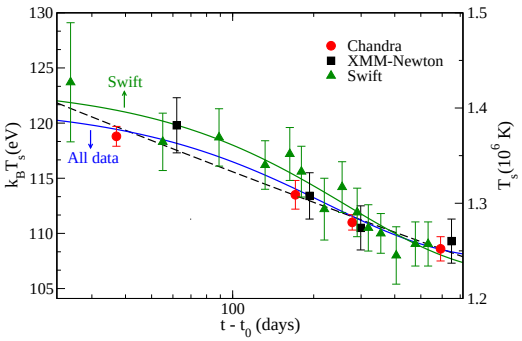

(c) **EXO 0748−676**, data and fits from Díaz Trigo et al. (2011) and Degenaar et al. (2011b).

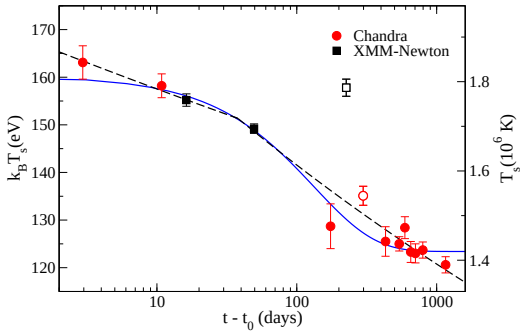

(d) **XTE J1701−462**, data and fits from Fridriksson et al. (2011). Data with open symbols (XMM-3 and CXO-4) were not considered in fits.

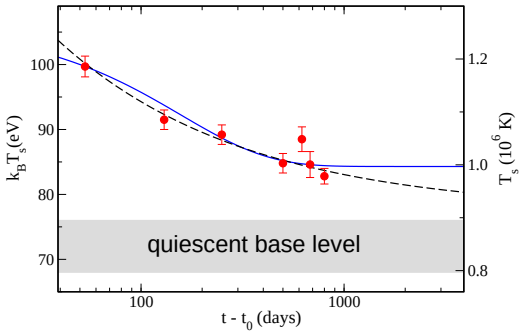

(e) **IGR J17480−2446**, data and fits from Degenaar et al. (2013).

Fig. 1. Observational data and corresponding fits taken from the literature. Data from *Chandra* (circles), *XMM-Newton* (squares) and *Swift* (triangles) for all the sources. Exponential decay $k_B T_s = a\ e^{-(t-t_0)/\tau} + b$ (solid lines), and (broken) power laws $k_B T_s = \alpha(t-t_0)^{\beta}$ (dashed lines) fits.

$a = (73 \pm 2)$ eV, $\tau = (465 \pm 25)$ d, and $b = (54 \pm 2)$ eV, with $\chi^2 = 0.8$ (Cackett et al. 2008). This fit shows that the flux and temperature of the last observation remained consistent with the previous two *Chandra* observations performed 1000 days before.

Recently a new *Chandra* observation (Cackett et al. 2013) showed an unexpected drop in count rate and a change in the spectral shape which cannot be explained by continued cooling. Two possible scenarios are discussed in that work: first, it is assumed that the NS temperature remained unchanged and there was an increase in the column density; alternatively, t he NS surface temperature dropped and the spectrum is now dominated by a power law component. Future observations of this source are necessary to

Table 1. Sources, average accretion rate $\dot{M}_{\rm obs,18}$ and accretion period $t_{\rm acc}$ inferred from observations. Coeficients for exponential ($k_BT_s = a\ e^{-(t-t_0)/\tau} + b$), power law ($k_BT_s = \alpha(t-t_0)^{\beta_1}$) and broken power law fits ($k_BT_s = \alpha(t-t_0)^{\beta_1}$, $k_BT_s = (t-t_b)^{\beta_2}$). References: [a] Cackett et al. (2008), [b] Cackett et al. (2010a) , [c] Degenaar et al. (2011b), [d] Díaz Trigo et al. (2011), [e] Fridriksson et al. (2011), and [f] Degenaar et al. (2013). † = Fit inconsistent with the last observation. †† = Fit considers a constant offset of $b = (77.3 \pm 1.0)$ eV.

Source	$\dot{M}_{\rm obs,18}$	$t_{\rm acc}$	Exponential fit				Power, broken power law fits			
	($\rm g\,s^{-1}$)	(yr)	a (eV)	τ (d)	b (eV)	χ^2	α (eV)	$\beta_1, \beta_2 \times 10^{-3}$	$t_{\rm b}$ (d)	χ^2
MXB 1659−29[a]	0.07-0.18	2.5	$73^{\pm2}$	$465^{\pm25}$	$54^{\pm2}$	0.8		—		
KS 1731−260[b]	0.05-0.3	12.5	$39.8^{\pm2.3}$	$418^{\pm70}$	$67.7^{\pm1.3}$	2.00†	$174.7^{\pm1.3}$	$\beta_1 = -12.5^{\pm7}$		0.88
EXO 0748−676	0.03	24								
Chandra[c]			$17.2^{\pm1.8}$	$266^{\pm100}$	$106.2^{\pm2.5}$	0.02		—		
Swift[d]			$13.4^{\pm0.2}$	$192^{\pm10}$	$107.9^{\pm0.2}$	0.34	$135.0^{\pm17.8}$	$\beta_1 = -30^{\pm30}$	$166^{\pm99}$	0.3
								$\beta_2 = -60^{\pm20}$		
XMM-Newton[d]			$17.2^{\pm5.8}$	$133^{\pm88}$	$109.1^{\pm2.2}$	0.06	$141.0^{\pm8.4}$	$\beta_1 = -40^{\pm10}$		0.4
all data[d]			$14.0^{\pm1.4}$	$220^{\pm65}$	$107.6^{\pm1.5}$	0.39	$135.8^{\pm2.5}$	$\beta_1 = -35^{\pm3}$		0.51
XTE J1701−462[e]	1.1	1.6	$36.9^{\pm1.7}$	133^{+38}_{-25}	$123.4^{\pm0.9}$	1.07	$168.8^{\pm5.7}$	$\beta_1 = -30^{\pm13}$	38^{+24}_{-12}	0.88
								$\beta_2 = -69^{\pm4}$		
IGR J17480−2446[f]	0.2	0.17	$21.6^{\pm4}$	$157^{\pm62}$	$84.3^{\pm1.4}$	1.84	$147.9^{\pm12.7}$	$\beta_1 = -47^{\pm5}$		1.2††

disentangle between these two possibilities (corresponding temperatures are shown as open symbols in Fig. 1a).

2.2. KS 1731−260

First detected in 1989 (Sunyaev & Kwant Team 1989), the presence of Type-I x-ray bursts identified this compact object as a NS. The source was actively accreting for 12.5 yr and the last detection in outburst was on January 2001 with a luminosity of $10^{36}\,\rm erg\,s^{-1}$ (Wijnands et al. 2001) with an inferred $\dot{M}_{\rm obs,18} \sim 0.1$ (Galloway et al. 2008).

Its first 4 years in quiescence were studied by Cackett et al. (2006); they analyzed *XMM-Newton* (XMM) and *Chandra* (CXO) observations and fit the data spectrum with an absorbed neutron star atmosphere (see Fig. 1b). In that work it was not clear if the source had reached the thermal equilibrium with the core, or if it was still cooling, but the last observation seemed to indicate the first. Then, the data were well fit in a first moment by an exponential decay to a constant offset ($a = (39.5 \pm 3.6)$ eV, $\tau = (325 \pm 101)$ d, $b = (70. \pm 1.6)$ eV, $\chi^2 = 0.2$).

Years later, Cackett et al. (2010a) presented a new Chandra observation that shows a decrease in the temperature, not consistent with the previous fit. Revision of all the *Chandra* and *XMM-Newton* data concluded that the source was still cooling with the temperature following a power-law decay (see Tab. 1). However, one problem in this analysis is that the spectrum may not be purely thermal and some non-thermal contribution could not be detected due to low number of counts. Observations are consistent with a simple NS atmosphere model, but a low level (less than 10%) contribution from a power-law cannot be excluded.

2.3. EXO 0748−676

The first detection of this source was in 1980 (Parmar et al. 1986) at luminosities $\sim 10^{36-37}\,\rm erg\,s^{-1}$ and it remained active for more than 24 years. The bursts rise time and duration suggested pure helium ignition. The transition from outburst to quiescence happened during 2008 and was monitored by Degenaar et al. (2009, 2011b) and Díaz Trigo et al. (2011) and they obtained a value for the mass accretion rate of $\dot{M}_{\rm obs,18} \sim 0.03$.

Degenaar et al. (2011b) discussed *Chandra* and *Swift* observations after its very long outburst and extended the monitoring made by Degenaar et al. (2009) to 19 months (Fig. 1c). They described the quiescent spectrum of EXO 0748−676 by assuming a combination of a NS atmosphere model plus a non-thermal power law tail (see Tab. 1) and concluded that there is a significant but gradual decrease in the NS effective temperature (from $\sim$ 124 eV to 109 eV) interpreted as crustal cooling. In this work they also observed that quiescent light curves present a shift between data thermal fluxes (of $\sim$ 6%) coming from the two satellites, apparently due to cross calibration issues. They presented fits for *Chandra* and *Swift* data separately (Tab. 1). Díaz Trigo et al. (2011) revisited the problem and analized *XMM-Newton* data, which are the most sensitive observations of the source. They found that *XMM-Newton* fluxes are compatible with *Swift*, which reaffirms the hypothesis of an offset in the calibration between *Chandra* and *Swift*.

Exponential fits indicate that the NS crust could be already close to the equilibrium with the core. The unabsorbed flux ($7.7 \times 10^{-13}\,\rm erg\,cm^{-2}\,s^{-1}$) detected in April 2010 by *Chandra* is close to the one measured by the EINSTEIN observatory prior to its last outburst ($8.4 \times 10^{-13}\,\rm erg\,cm^{-2}\,s^{-1}$), supporting the idea that the crust has reached thermal equilibrium. Nevertheless, it is worth to notice that the amount of cooling following the end of the outburst is markedly smaller with respect to the other sources.

2.4. XTE J1701−462

The neutron star transient XTE J1701−462 was discovered in 2006 (Remillard et al. 2006) and remained in an exceptional luminous outburst for about 19 months. The transition from outburst to quiescent emission and the first 800 days of the quiescent phase were first monitored by Fridriksson et al. (2010). During most of the quiescent period, the source was followed by *Chandra* in a campaign consisting of 10 observations made between August 2007

and October 2009, and, lately, one more in October 2011. It was also observed three times with *XMM-Newton* in August 2007, September 2007 and March 2009, and last data came from April 2011 taken from *Swift* (Fridriksson et al. 2010, 2011). Data points are shown in Fig. 1d. The inferred value for the mass accretion rate is close to the Eddington rate, $\dot{M}_{\rm obs,18} = 1.1$ (Cackett et al. 2010b). Its luminosity was measured very early in the quiescent phase: three data points in the first twenty days, which gives valuable information about the cooling right after the end of the outburst.

Spectra of XTE J1701−462 show thermal and non-thermal components with the latter well fitted by a power law of index 1-2. The origin of the non-thermal emission is not well understood but it is likely coming from magnetospheric activity (Campana et al. 1998). The thermal emission in quiescence (see Fig. 1d), shows a temperature decrease interpreted as the cooling of the NS crust heated up in the accretion phase. Nevertheless, some features in the observed luminosity indicate that the peculiar crustal cooling may be affected by other processes.

First, we note that the effective surface temperature decreases from approximately 160 eV to 120 eV, significantly higher temperatures than those inferred for MXB 1659−29 and KS 1731−260 (approx. from 120 eV to 60 eV). The relatively warm surface of XTE J1701−462 may be a result of the high (close-to-Eddington) accretion rate at which this source has been accumulating matter most of its active phase. Alternatively, it could also be due to a higher core temperature (may be it is a young star?).

Second, the overall cooling rate seems to be explained by crustal heating, as analyzed in Fridriksson et al. (2011) from data from *XMM-Newton* and *Chandra* where they found good fits considering exponential and broken power law functions with $\chi^2 = 1.07$ and $\chi^2 = 0.88$, respectively. However, these fits do not include the third *XMM-Newton* (XMM-3) and the fourth *Chandra* (CXO-4) observations between $\sim 200 - 300$ days, which show a considerable increment in thermal and non-thermal spectral components (Fridriksson et al. (2011), see Tab. 1).

One more drawback is that in Fridriksson et al. (2010) it was not clear if the XTE J1701−462 crust had already reached a thermal equilibrium with the core. A very recent Chandra observation indicated, with 80% confidence, that the surface temperature has decreased, implying that the source is still cooling (Fridriksson et al. 2011), which is inconsistent with previous fits.

Another challenge for crustal cooling models is that the temperatures registered at early times drop in a relatively short timescale with an *e*-folding time for the exponential fit of ∼120 days (in comparison with ∼300 days and ∼460 days for MXB 1659−29 and KS 1731−260, respectively (Cackett et al. 2010a)) which argues in favor of a highly conductive crust. Moreover, the temperature evolution shows a change in the slope at around 80-100 days (Fridriksson et al. (2011) obtained even 25-80 days). This *break* in the evolution makes difficult to reconcile the initial rapid cooling showed by early observations and the much slower decrease from the last data in the same cooling model.

2.5. IGR J17480−2446

The transient IGR J17480−2446 was found in the globular cluster TERZAN by *Chandra* telescope in 2003 (Heinke et al. 2006). In October 2010 it suddenly entered in an outburst period increasing its intensity by ∼1 order of magnitude (Bordas et al. 2010; Pooley et al. 2010). The source returned to quiescence after ∼ 10 weeks (Degenaar & Wijnands 2011a). A *Chandra* observation 50 days after the end of the outburst showed that the surface temperature was higher than the base level observed in 2003 and 2009 by a factor 4 (Degenaar & Wijnands 2011b).

Very recently, Degenaar et al. (2013) reported new *Chandra*/ACIS observations on IGR J17480−2446 that extend the monitoring to 2.2 years into quiescence. They found that even when the thermal flux and NS temperature have decreased, their values still remain well above those measured in the previous accretion phase. They fitted these last observations with exponential decays and found that when the quiescence base level is fixed to the temperature inferred from 2003/2009 data, fits results are pour ($\chi^2 \sim 3$), however, it is considerably improved ($\chi^2 \sim 1.84$) if this parameter varies freely, in which case the base level is $b = (84.3 \pm 1.4)$ eV, considerably higher than the quiescent level. As this value is close to the obtained from the previous observation in 2013 February, this predicts that the NS crust has nearly leveled off (see solid curve in Fig. 1e). Nevertheless the best fit corresponds to a power law decay with a free base level, for which $b = (77.3 \pm 1.0)$ eV, significantly lower than the most recent observation (see dashed curve), pointing into continued cooling of the crust.

2.6. Sources comparison

We now briefly compare here the observational characteristics of the five sources in quiescent emission detected so far (refer to Fig. 1 and Tab. 1). We can group MXB 1659−29 and KS 1731−260 together since they have similar accretion rates ($\sim 0.1 M_{18}$), evolve in a similar temperature range ($\sim 120-60$ eV) and in comparable timescales (~ 2000 days) are (nearly) leveled off with the core. Their data spectra are well fitted with an absorbed NS atmosphere and their exponential fits show that the e-folding time is similar, $\sim$ 500 days and $\sim$ 400 days for MXB 1659−29 and KS 1731−260, respectively. Although the data are sparse in time, the observational data points show relatively low error bars.

On the contrary, EXO 0748−676 and XTE J1701−462 (and partially IGR J17480−2446) present some peculiar characteristics. First, their surface temperatures indicate that these objects are warmer than those in the first group. Data points show in general much higher variability, with larger error bars, specially the *Swift* and *Chandra* data for EXO 0748−676. In addition, their e-folding times are considerably smaller: ∼130 and ∼220 days for XTE J1701−462 and EXO 0748−676, respectively. The temperature variability as these sources cool down differs considerably from the first two: $\sim (125-110)$ eV for EXO 0748−676, $\sim (170-120)$ eV for XTE J1701−462. Note that EXO 0748−676 has the smallest accretion rate ($\sim 0.01 M_{18}$) but the longest accretion time ($\sim$ 24 yrs), which can be the origin of its high surface temperature. More puzzling is the small amount of cooling that it shows, its temperature falls only $\sim$ 10 eV from the initial to the equilibrium temperatures.

Table 2. NS configurations used in this work: mass M, central density ρ_0, stellar radius R, surface gravity g and crust width ΔR_c

M ($M_\odot$)	ρ_0 (10^{14} g cm^{-3})	R (km)	g (10^{14} cm s^{-2})	ΔR_c (m)
1.4	9.88	11.79	1.34	944
1.6	11.65	11.61	1.58	735
1.8	14.40	11.31	1.88	569

XTE J1701−462 instead, has the largest accretion rate, at least ten times higher than the other sources. The pronounced break between the early and latest observations slope is not evident in the other sources.

Finally, IGR J17480−2446 shows similarities to the first group, like an accretion rate of the same order, but has the shortest accretion time among all sources. It exhibits a small e-folding time $\sim$ 60 days like EXO 0748−676 and XTE J1701−462 but with a temperature variability in the overall cooling of only $\sim$(100-80) eV.

Another point to remark is that first observations for KS 1731−260, MXB 1659−29, EXO 0748−676 and IGR J17480−2446 were performed not before 25 days after the end of the outburst. Thus, important information about the first stage of cooling of these sources is missed. Conversely, XTE J1701−462 was observed three times in the first 20 days (the first observation was only 3 days after the end of the outburst). The existence of these early data is a qualitative difference with respect to MXB 1659−29 or KS 1731−260. In particular, it carries important details about the physics of the outer layers of the NS, which are directly involved in the after-burst cooling. Contrarily, EXO 0748−676 has an uncertain date for the end of the outburst phase, being poorly constraint in a period of 7 weeks Degenaar et al. (2011b).

3. Baseline model

3.1. Equation of state.

At low density we use the BBP Baym et al. (1971) equation of state. The crust-envelope interface is placed at $(5-6)\times10^8$ g cm^3 and we continue using BBP EoS to describe the crust up to the density 1.49×10^9 g cm^{-3}. To take into account the effects of the accretion in the crust composition, we use the EoS presented in HZ08 in the range $\rho = (1.49\times10^9 - 3.5\times10^{13})$ g cm^{-3}. This is a BBP-like EoS but modified by non-equilibrium nuclear reactions in the crust (see next Section). To describe the very high density region in the inner crust and the core we use Douchin & Haensel (2001), a Skyrme-type EoS which considers a nucleon-nucleon SLy effective interaction. For this chosen EoS the crust-core interface is at 0.5 ρ_0, where $\rho_0 = 2.8\times10^{14}$ g cm^{-3} is the nuclear saturation density.

Throughout this paper we use three different NS models with masses: $M = 1.4$ M$_\odot$, 1.6 M$_\odot$ and 1.8 M$_\odot$. Their properties are listed in Tab. 2 where we can observe how the crust width decreases as the mass increases; as we will show later this directly influences the crustal relaxation time.

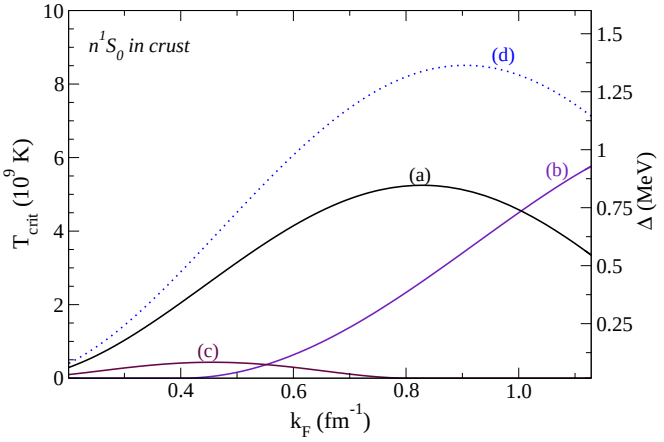

Fig. 2. Fermi momentum dependence of the critical temperature and gaps $\Delta(T=0)$. The neutron singlet gap is related with the critical temperature by $T_{\rm crit} = 0.56\Delta(T=0)$ (see right axis). References: (a) Sch03 gap (Schwenk et al. 2003); (b) deep gap; (c) small gap; (d) Wambach et al. (1993)

Table 3. Parametrization and references of the energy gaps for superfluid states

Label	Δ_0 (MeV)	k_0 (fm^{-1})	k_1 (fm^{-1})	k_2 (fm^{-1})	k_3 (fm^{-1})
a	72.7	0.1	6.2	1.5	2.79
b	4.0	0.4	1.5	1.65	0.05
c	20.7	0.1	6.2	1.5	2.79

References. (a) Sch03 gap; (b) deep gap; (c) small gap

3.2. Superfluidity

Nucleon pairing does not affect the EoS but it can play an important role in NS cooling since it strongly modifies the specific heat and neutrino emissivities of dense matter. Following Kaminker et al. (2001) and Andersson et al. (2005), we use a phenomenological formula for the momentum dependence of the neutron energy gap at zero temperature given by

$$\Delta(k_F) = \Delta_0 \frac{(k_F-k_0)^2}{(k_F-k_0)^2+k_1}\frac{(k_F-k_2)^2}{(k_F-k_2)^2+k_3} \quad (1)$$

where $k_F = (3\pi^2 n)^{1/3}$ is the Fermi momentum of neutrons and the parameters Δ_0 and k_i, $i = 1..4$ are values fitted to microphysical calculations listed in Tab. 3. This expression is valid for $k_0 < k_F < k_2$, with vanishing Δ outside this range.

The Fermi momentum dependence of the gaps is plotted in Fig. 2. The bare interaction predicts a maximum gap $\Delta^{\rm max} \simeq 3$ MeV (Schulze et al. 1998), but polarization effects reduce it by a factor 2-3. The corresponding critical temperatures for the s-wave can be approximately calculated as $T_{\rm crit} = 0.56\,\Delta(T=0)$. It is important to remark that at high densities the crustal temperatures for the five sources studied in this work are always lower than the corresponding critical temperatures. Thus, neutrons are already in a superfluid state in the inner crust. Unless otherwise

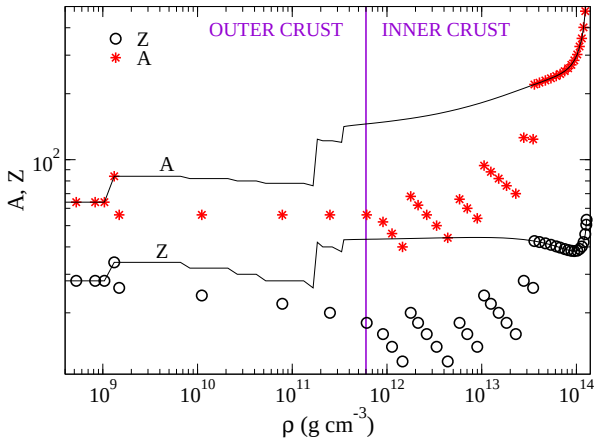

Fig. 3. Accreted crust composition (stars, circles) for $^{56}F_{\rm e}$ burning ashes (HZ08) in comparison to the non-accreted crust (solid lines) (Douchin & Haensel 2001).

stated, we consider the parameters set by Schwenk et al. (2003) in our simulations.

3.3. Crust composition

The crust of an accreting NS can be entirely replaced after an accretion period of several years. Thus, its composition can be significantly different from that of isolated NSs, as we can see in Fig. 3 (HZ08, BC09), which shows the mass number A (circles) and the nuclear charge Z (stars) as a function of the density along the NS crust assuming that initial ashes are $^{56}F_{\rm e}$; solid lines denote the non accreted composition. We refer to Sec. 2.1 of HZ08 for details about the capture rates in different regimes.

In the inner crust, at densities above the neutron drip density, $\rho_{\rm ND} \sim 3\times10^{11}\,{\rm g\,cm^{-3}}$, there are neutron emissions in addition to electron captures which makes A to decrease. This happens until high enough densities at which the Coulomb barrier gets lower; at this point the mean distance between nucleus diminishes and quantum zero-point vibrations increase leading to pycnonuclear reactions which results in jumps in A. In Fig. 3 we can observe that the composition changes abruptly with depth, the jumps correspond to the location of thresholds for pycnonuclear reactions.

3.4. Transport properties and neutrino emission

The processes that dominate the crust thermal conductivity depend (strongly) on temperature and density. While electron-phonon scattering dominates at low densities in the outer crust, electron-impurity scattering is the most important process at higher densities in the inner crust. To calculate these processes, we used the public code of A. Potekhin[3].

[3] http://www.ioffe.rssi.ru/astro/conduct/condmag.html

An important, but uncertain, parameter in the calculation of the thermal conductivity is the impurity parameter, defined as:

$$Q_{\rm imp} = Z^2_{\rm imp} = n_{\rm ion}^{-1}\sum_{\rm i} n_{\rm i}(Z_{\rm i} - \langle Z\rangle)^2 \qquad (2)$$

Large values of this parameter ($Q_{\rm imp} \sim 100$) correspond to an amorphous crust and a low thermal conductivity. Recent molecular dynamic calculations, however, predict a regular crystalline structure with a moderate value of $Q_{\rm imp}$ of the order of unity (Horowitz et al. 2007, 2009) in the outer crust. BC09 estimated the value of $Q_{\rm imp}$ by fitting the observational data of the sources KS 1731−260 and MXB 1659−29 and found also that $Q_{\rm imp} \sim 1-5$.

Another important quantity is the specific heat. In normal non-superfluid NS matter, the major contribution is due to nucleons in the core. One important feature of the nucleons specific heat is that it is suppressed by nucleon pairing in the inner crust and core. Thus, neutron contributions in the inner crust (where the pairing state is n^1S_0) are suppressed by a factor $\mathcal{R}^{cv}$, which depends on the pairing gap (Levenfish & Yakovlev 1994). The specific heat contributions also depend (strongly) on the temperature and (less strongly) on the density: it is dominated by the ion lattice at low density and by free neutrons and electrons at high density.

We also include all relevant neutrino emission processes that influence the cooling of the crust (see Tab. 3 in Aguilera et al. (2008) for a list.) At high temperatures ($T \simeq 10^9$ K) the dominant process is the plasmon decay, at intermediate values ($T \simeq 5\times10^8$ K) plasmon decay is only dominant in the outer crust, while electron-nuclei Bremsstrahlung becomes more efficient in a large part of the crust volume (Yakovlev et al. 2001). We also include the Cooper Pair Breaking an Formation (CPBF) process which is dominant in a narrow region of the inner crust.

4. Thermal evolution

Once we have defined the baseline NS model, we follow its thermal evolution by solving the diffusion equation taking into account all energy gains and losses:

$$c_{\rm v}\frac{\partial T}{\partial t} = -\nabla\cdot F + Q_\nu + Q_{\dot m}, \qquad (3)$$

where $c_{\rm v}$ is the specific heat per unit volume, Q_ν denotes the energy loss by neutrino emissions and $Q_{\dot m}$ considers energy gains as a consequence of the accretion of matter. Specifically, as we mentioned in Sec. 3.1, the deep crustal heating considers that there are heat sources located in the inner crust[4] due to the occurrence of pycnonuclear reactions and electron captures. The heat flux F is given by the following expression:

$$F = -k\nabla T \qquad (4)$$

where k is the thermal conductivity tensor, that includes contributions of electrons, neutrons, protons and phonons:

$$k = k_{\rm e} + k_{\rm n} + k_{\rm p} + k_{\rm ph} \qquad (5)$$

[4] In Sec. 10.1 we will also explore the presence of additional heat sources in the outer crust.

The electronic term is dominant in the crust, while radiative transport is the most important process close to the surface.

The temperature evolution is followed in the region that extends from the crust-core interface ($\rho_{\rm cc} = 1.3 \times 10^{14}\,{\rm g\,cm^{-3}}$) down to the base of the envelope (crust-envelope interface at $\rho_{\rm b} = 5.6 \times 10^{8}\,{\rm g\,cm^{-3}}$).

4.1. Crustal heating during outbursts: generating the initial thermal profile

To simulate the accretion phase, we consider the heat released per nucleon as a function of the density (as in HZ08, Sec. 3.3). The integration in Eq. 3 is performed until the temporal variable equals the duration of the outburst. At this time, the NS crust has reached a thermal profile that depends on the local energy release per nucleon, the local accretion rate $\dot{m}$, and the duration of the outburst $t_{\rm acc}$. Then, the quiescent phase begins and the NS crust starts to cool down from this *initial* thermal profile, that corresponds to the conditions at the end of the outburst.

4.2. Inner boundary: the core

The equilibrium temperature of the system is set by the core temperature, T_c, which depends mainly on the long-term averaged accretion rate. We assume that the recurrence time, i.e. the time between two accretion events, is small compared to the relaxation time of the core ($\sim 10^3$ yr) and the source has gone through several accretion-quiescence cycles so the core has reached thermal equilibrium and its temperature remains roughly constant. Thus, as an inner boundary condition, we fix T_c to a constant value being this a free parameter to fit the observations. If the NS has reached the thermal equilibrium with the core, T_c will be determined by the last observations. Otherwise, if the source is still cooling T_c is difficult to infer.

We have checked that assuming a constant T_c is a good approximation for quasi-persistent sources unless accretion lasts for much longer than ~ 10 yrs. In that case, the core could be heated up by an inward flux generated due to the strong heat deposition over the extended period (e.g. for EXO 0748−676 if $t_{\rm acc} \sim 100$ yrs).

4.3. Outer boundary: the envelope

To study the thermal evolution of the crust, the outer boundary condition presents numerical difficulties since the external layers have a thermal relaxation time (∼1-100 s) much shorter than the crustal cooling timescale (∼1000 days). Therefore we assume that the crust is surrounded by a fully relaxed envelope and we treat the two regions separately. The outer limit of integration for the crustal cooling is then the bottom of the envelope, with temperature $T_{\rm b}$, which is determined by thermonuclear reactions during outburst. In this sense, the initial value of this temperature, $T_{\rm b}^0 = T_{\rm b}(t = t_0)$ contains relevant information about the heating of the envelope during the active phase.

Nevertheless, in the simulations presented in the literature, $T_{\rm b}^0$ was set as a free parameter to fit the first observations in quiescence (e.g. in BC09 for MXB 1659−29 and KS 1731−260). In the present work, instead, we obtain stationary solutions of the envelope during outburst and derive a relation between $T_{\rm b}^0$ and the accretion rate $\dot{M}$ (see Sec. 5.2); this allows us to connect the physics of the outburst with the quiescent emission in a more consistent way. Moreover, the number of free parameters used to describe the problem is reduced and, as we will show, this opens the possibility to constraint the envelope composition.

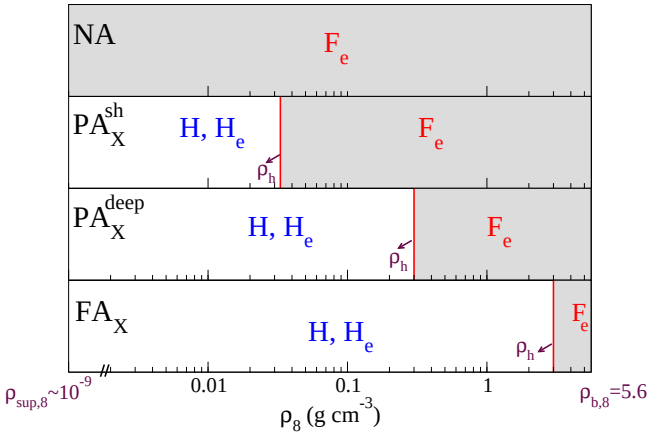

Fig. 4. Envelope models used: non-accreted (NA), partial accreted with light elements at shallow density ($\mathrm{PA_X^{sh}}$) and at deep density ($\mathrm{PA_X^{deep}}$), and fully accreted envelope (FA).

5. Envelope models

Here we describe how to obtain the envelope stationary solutions for a given $T_{\rm b}^0$; this defines the $T_{\rm b}$–$T_{\rm s}$ relation to be used as the outer boundary condition for the thermal evolution of the crust.

5.1. The envelope in quiescence

The envelope is assumed to be composed by light elements (H and ^{4}He) for densities from $\rho_{\rm sup} \simeq 0.3$ g cm^{-3} (outer limit of integration), up to $\rho_{\rm h}$, which demarcates the presence of heavier elements. Beyond this light/heavy elements interface, we assume a layer of pure ^{56}Fe up to the envelope-crust interface at $\rho_{\rm b}$ (inner limit of integration). The density $\rho_{\rm h}$ is highly uncertain and to analyze its influence on upcoming results we consider three different models (see Fig. 4 and Tab. 4):

- a non-accreted envelope (NA), for which $\rho_{\rm h} \simeq \rho_{\rm sup}$,
- a partially accreted envelope (PA), with $\rho_{\rm sup} \ll \rho_{\rm h} \ll \rho_{\rm b}$; we vary the location of $\rho_{\rm h}$ defining a *deep* ($\mathrm{PA^{deep}}$ with $\rho_{\rm h,8} = 0.33$) or a *shallow* ($\mathrm{PA^{sh}}$ with $\rho_{\rm h,8} = 0.045$) partial accreted model,
- and a fully accreted envelope (FA), with $\rho_{\rm h} \simeq \rho_{\rm b}$,

where $\rho_{\rm h,8}$ is $\rho_{\rm h}$ in units of $10^8\,{\rm gr\,cm^{-3}}$. Moreover, for accreted models, we vary the H and He fraction denoted by X and $Y = 1 - X$ and we label them with the corresponding H percentage, e.g. $\mathrm{PA}_{X\%}$, $\mathrm{FA}_{X\%}$.

The $T_{\rm b}$–$T_{\rm s}$ relations obtained are shown in Fig. 5. At low $T_{\rm b}$ the PA model converges to the FA model. For high $T_{\rm b}$,

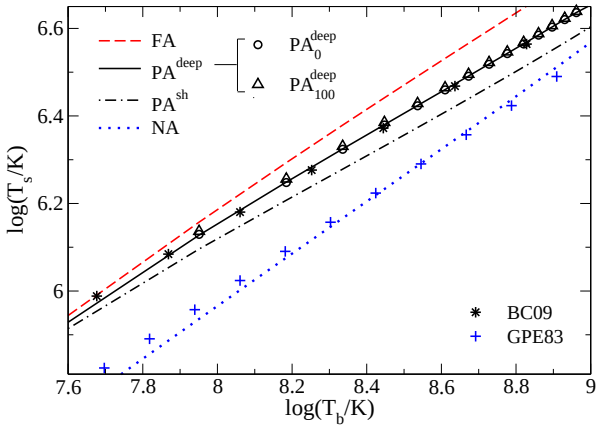

Fig. 5. $T_{\rm b}$–$T_{\rm s}$ relations for envelope models: dashed line for FA, solid line for $\mathrm{PA^{deep}}$, dashed dotted line for $\mathrm{PA^{sh}}$ and dotted line for NA. Comparison of PA models with BC09 (stars) and of NA model with GPE83 (crosses).

Table 4. Coefficients of the fits for $T_{\rm b}$–$T_{\rm s}$ relations for NA, PA, and FA envelope models. Corresponding density and depth for heavy elements are $\rho_{\rm h,8}$ and $y_{\rm h,11}$.

Model	$\rho_{\rm h,8}$	$y_{\rm h,11}$	$\log(T_{\rm s}/{\rm K}) = a + b\log(T_{\rm b}/{\rm K})$	
NA	~ 0	~ 0	$a = 1.14$	$b = 0.60$
$\mathrm{PA^{sh}}$	0.045	0.013	$a = 2.16$	$b = 0.49$
$\mathrm{PA^{deep}}$	0.3	0.1	$a = 2.15$	$b = 0.50$
FA	3.0	4.0	$a = 1.70$	$b = 0.57$

however, it resembles the NA model. As we show, these relations do not depend appreciably on the H fraction within a model (circles for $\mathrm{PA_0^{deep}}$ and triangles for $\mathrm{PA_{100}^{deep}}$). We can also compare solutions with previous results: for the $\mathrm{PA^{deep}}$ model the value of $\rho_{\rm h,8} = 0.3$ was chosen in order to reproduce the relation used in BC09 (stars) and to facilitate comparison of the cooling curves in upcoming sections. We also consider the canonical relation for the non-accreted case (Gudmundsson et al. (1983), hereafter GPE83), which is in very good agreement with our NA model.

We linearize these relations in a log-log plot and show corresponding coeficients in Tab. 4, where for each $\rho_{\rm h,8}$ we give the corresponding depth, $y_{\rm h,11}$ in units of 10^{11} gr cm^{-2}.

As we noticed before, these results are very weakly dependent on the fraction of light elements in the envelope; what is more important is the value of the density $\rho_{\rm h}$. Note that, although these relations depend on the value used for $\rho_{\rm b}$, cooling curves do not. This is because we keep $\rho_{\rm b}$ to have the same value as the lower limit of integration in the time-dependent code and as the upper limit in the stationary version.

5.2. Heating of the envelope in the accretion phase

When matter is accreted and reaches the surface of a NS, the outer layers are continuously compressed by the new material and eventually they reach the pressure and temperature necessary to induce thermonuclear ignition. The total energy released (most due to the fusion of hydrogen to helium) depends on the envelope composition and the accretion rate (typically $\dot{M} \sim 10^{(14-18)}\,{\rm g\,s^{-1}}$) and determines the envelope thermal state. Therefore, there is a relation between $T_{\rm b}^0$ and $\dot{M}$. We solve the NS envelope thermal structure, as in the former section, but now considering the heat produced by thermonuclear reactions in the envelope as included in $Q_{\dot{\rm m}}$.

Following Bildsten (1997), we assume steady-state equilibrium burning, ie. the matter burns at the same rate it is accreted. In such scenario, we can define the steady-state heating flux as: $F = E_{\rm nuc}\dot{m}$, where $E_{\rm nuc}$ is the nuclear energy released per unit of mass. During the calculations, we assume a fixed envelope composition, ie. the light elements abundances do not depend on density and time, so we do not track the evolution of the envelope composition during burning. In order to do that it would be necessary to solve a continuity equation for each element in a consistent way with the heat diffusion equation, which is far beyond the scope of this work.

During burning, most of the released energy is due to the fusion of H and He to heavier elements. Two reactions dominate the generation of energy: the hot CNO cycle and He burning through the triple alpha reaction. For global accretion rates in the interest range, i.e $\dot{M}_{18} \sim 0.01 - 1.00$, the temperature and density of the burning zone are high enough to activate the hot CNO cycle. This cycle is slightly different from the CNO: it is *not* temperature dependent, and hence it is stable against thermal perturbations. Its energy generation rate is:

$$\epsilon_{\rm h} = 5.8 \times 10^{15} Z_{\rm CNO}\ {\rm erg\,g^{-1}\,s^{-1}}, \tag{6}$$

where $Z_{\rm CNO}$ is the mass fraction of CNO in the accreting matter.

The other relevant process is the He burning which has an energy generation rate of

$$\epsilon_{3\alpha} = 5.3 \times 10^{21} \rho_5^2\, Y^3\, \frac{\exp(-44/T_8)}{T_8^3}\ {\rm erg\,g^{-1}\,s^{-1}} \tag{7}$$

where Y is the helium abundance and ρ_5 is the density in 10^5 g cm^{-3}. This process can lead to unstable burning since it is temperature-dependent.

Knowing the energy generation rate for light elements burning, we can calculate the depth y at which light elements burns. In a steady-state scenario, a light element depletes at the depth where the time it takes for an element to cross a characteristic distance equals the time it takes to burn:

$$\begin{aligned} E_{\rm nuc,H}\,\dot{m}\,X &= \epsilon_h\, y_{\rm H} \quad \text{for} \quad \text{H} \\ E_{\rm nuc,He}\,\dot{m}\,Y &= \epsilon_{3\alpha}\, y_{\rm He} \quad \text{for} \quad \text{He} \end{aligned} \tag{8}$$

Hence, the burning depth of H and He ($y_{\rm H}$ and $y_{\rm He}$, respectively) depends on the energy generation rate, the envelope composition and the accretion rate; these parameters determine whether the burning regime is stable or unstable. Thus, solving Eq. 8 we get $y_{\rm H}$ and $y_{\rm He}$ which determine the heat sources location necessary to solve the stationary version of Eq. 3.

Stationary thermal profiles corresponding to $\mathrm{PA_{30}^{deep}}$ envelope model (solid curves) for different accretion rates $\dot{M}_{18} = 0.05 - 0.7$ are shown in Fig. 6. The region between dashed lines corresponds to unstable He burning (see Sec. 3

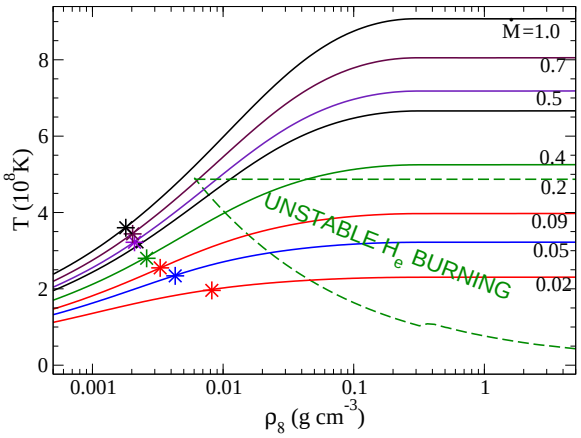

Fig. 6. Stationary thermal profiles for $\mathrm{PA}_{30}^{\mathrm{deep}}$. Stars show the density and temperature at which light elements burning occurs. In the region between dashed lines He burning is unstable.

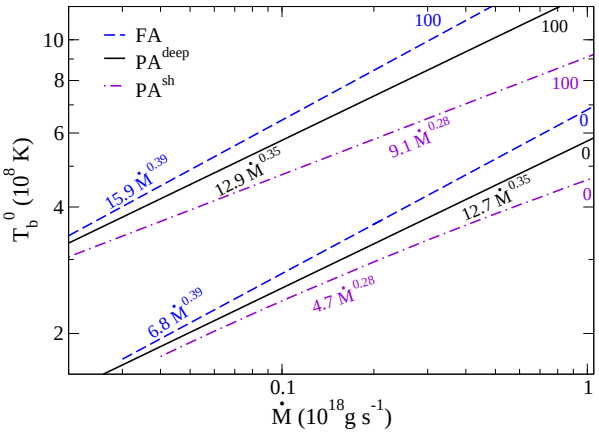

Fig. 7. $T_{\mathrm{b}}^0(\dot{M})$ relations: T_{b}^0 increases with $\dot{M}$ and the H fraction (0 - 100). Regressions with $T_{\mathrm{b},8}^0 = a\dot{M}_{18}^{0.28-0.39}$, see Tab. 5.

of Bildsten (1997)); we also indicate with stars the density at which light elements burning begins. The intersection of solid curves with the lower branch of the dashed line determines the He ignition temperature and density. The higher the accretion rate, the lower the burning depth, and for $\dot{M}_{18} > 0.7$, the envelope temperature is high enough for He stable burning. At high accretion rates, $\dot{M}_{18} \gtrsim 1$, $y_{\mathrm{H}} > y_{\mathrm{He}}$ and He burns stably before H. At low accretion rates, $\dot{M}_{18} \sim (0.01-1)$, He burns unstably in a mixed He/H interface and it triggers H burning. For even lower accretion rates, He burns after complete H burning in a pure He environment. At accretion rates lower than $\dot{M}_{18} \lesssim 0.01$, the temperature dependent CNO cycle dominates again and H burns unstably.

When the burning becomes unstable, we should solve the non-stationary diffusion equation and consider the temporal evolution of the elements abundances. Nevertheless in't Zand et al. (2009) studied the long tails observed in the source GS 1826-24 and found that the temperature in burst tails is determined by the initial (i.e before burst) NS temperature. In their Fig. 11 they showed that the temperature beyond depths $\sim 10^8\,\mathrm{g\,cm^{-2}}$ inside the star ($\sim 7\times10^5\,\mathrm{g\,cm^{-3}}$ in our configurations), remains roughly constant during all the unstable processes taking place in outer layers. Based on these facts, we assume that T_{b}^0 depends only on the accretion rate and it is not modified by the unstable ignition of light elements that might occur in the envelope.

In Fig. 7, we show $T_{\mathrm{b}}^0(\dot{M})$ relations obtained for different PA and FA envelope models by varying light elements abundances, plotting results for a pure He envelope (PA_0) and a pure H envelope (PA_{100}). As we mentioned before, the released energy by nuclear reactions depends strongly on these abundances, the higher the H fraction, the more energy is released and the higher value for T_{b}^0 (Fig. 7). Results can be well fitted with functions $T_{\mathrm{b},8}^0(\dot{M}) = a\dot{M}_{18}^{\gamma}$, where a and γ are coefficients given in Tab. 5. As we will see in the next sections, the use of the $T_{\mathrm{b}}^0(\dot{M})$ relation in the cooling curves will allow us to constraint the envelope composition by fitting the observations; this is one of the main goals of this work. It is worth noticing that these relations $T_{\mathrm{b}}^0(\dot{M})$ also depend on the NS mass through the NS crust width; results do not vary qualitatively but the fitting coefficients are slightly different.

Table 5. Envelope models $\mathrm{PA}_{\mathrm{X}}^{\mathrm{deep}}$ varying the composition X and corresponding energy released per nucleon E_{nuc}. Coefficients for the regression $T_{\mathrm{b},8}^0(\dot{M}) = a\dot{M}_{18}^{\gamma}$ for a 1.6 $\mathrm{M}_\odot$ NS.

Model	E_{nuc} (10^{18} erg g^{-1})	a (K s g^{-1})	γ
FA_0	0.58	6.8	0.39
FA_{100}	5.00	15.9	0.39
$\mathrm{PA}_0^{\mathrm{deep}}$	0.58	5.7	0.35
$\mathrm{PA}_{15}^{\mathrm{deep}}$	1.30	7.7	0.35
$\mathrm{PA}_{30}^{\mathrm{deep}}$	2.08	9.0	0.35
$\mathrm{PA}_{50}^{\mathrm{deep}}$	3.08	10.2	0.35
$\mathrm{PA}_{100}^{\mathrm{deep}}$	5.00	12.9	0.35
$\mathrm{PA}_0^{\mathrm{sh}}$	0.58	4.7	0.28
$\mathrm{PA}_{100}^{\mathrm{sh}}$	5.00	9.1	0.28

6. Revisiting crustal cooling

We now turn to discuss our results, that have been previously confronted with existing works (see details in Appendix A) for testing purposes.

6.1. Deep crustal cooling model: testing MXB 1659−29

We begin with MXB 1659−29, considered the most standard case. We use model 2 of Tab. 2, a NS with a mass of 1.6 $\mathrm{M}_\odot$ and radius $R = 11.79$ km, taking the impurity parameter Q_{imp}, the accretion rate $\dot{M}_{18}$ and core temperature $T_{\mathrm{c},8}$ as free parameters. The temperature evolution at the outer boundary, T_{b}, during outburst and quiescence,

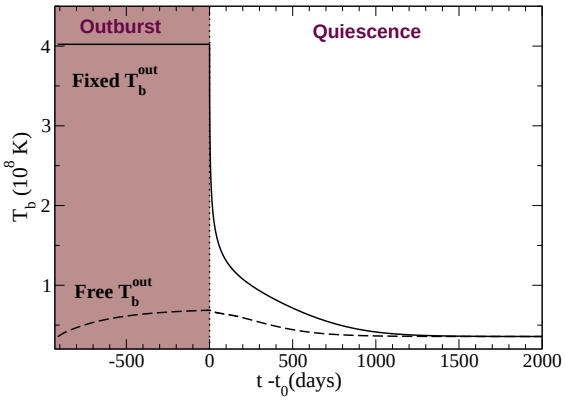

(a) Temperatures at the crust-envelope interface

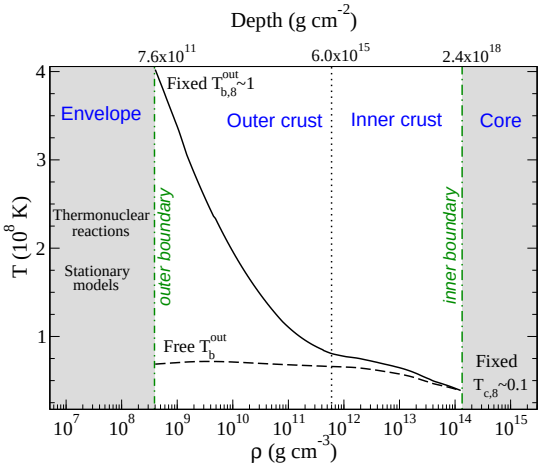

(b) Initial thermal profiles ($t = t_0$)

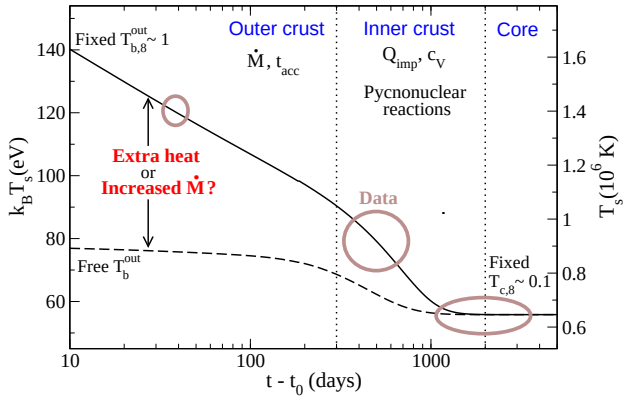

(c) Cooling curves

Fig. 8. Thermal evolution considering fixed (solid lines) or free (dashed lines) temperature during outburst T_b^{out}.

the corresponding initial thermal profiles and cooling curve are plotted in Figs. 8*a*, 8*b* and 8*c*, respectively.

First, we assume that the temperature at the base of the envelope during outburst, $T_b^{out}(t \leq t_0)$, is fixed to $T_{b,8}^{out} \sim 1$ (Fig. 8, solid lines) while at the inner boundary the core temperature is kept fixed to $T_{c,8} \sim 0.1$, both values chosen to fit the first and the last observations, respectively[5]. Note that the initial thermal profile suitable to explain the data (brown ellipses in Fig. 8*c*) has an inverted temperature gradient and hence an inward-directed heat flux as explained in detail in BC09. As it was assumed there, the (arbitrary) value of $T_b^0 \equiv T_b^{out}(t = t_0)$ is crucial to explain the early decay. To illustrate this point we plot the case when $T_{b,8}^{out}(t \leq t_0)$ is not held fixed, but instead, it evolves freely (dashed curves) controlled only by deep crustal heating (HZ08). Such curves fail to explain observations in the early cooling and a larger value of T_b^0 is necessary, as we can see from cooling curves (Fig. 8*c*).

At each time, the surface temperature reflects the initial conditions at a particular depth. Deeper, the crust did not have time to relax and exhibits roughly the initial thermal profile. Thus, each depth (or density) corresponds to an evolutionary time. The early cooling (first ~ 300 days) is controlled by the physics of the outer crust and the initial thermal profile, which depends strongly on $\dot{M}$ and on t_{acc} (see Eqs. 10-11 of BC09). The following epoch corresponds to the inner crust thermal relaxation, (approx. $\sim (300-1000)$ days) and is determined by electron-impurity scattering. After ~ 400 days the suppression of the neutron gas specific heat by nucleon pairing is evidenced by the temperature fall and the subsequent slope is mostly controlled by the pairing gap strength: a big energy gap suppresses the specific heat more efficiently causing an steeper fall. The cooling curve tail reflects the core thermal state (at $t \gtrsim 1000$ days) which temperature remains nearly constant. We have checked that the core temperature is not modified, unless the accretion period lasts for about 100 yrs.

6.2. Heated up envelope or wrong accretion rate?

To show how critical is the value of T_b^0 for the early decay, we also explore the case with $T_b^{out}(t \leq t_0)$ freely evolving. BC09 estimated that its value cannot rise to 10^8 K only by means of deep crustal heating (HZ08 sources) and that the required energy release in the outer crust is $\simeq 0.8\,\mathrm{MeV\,nuc^{-1}}$ for $\dot{M}_{18} = 0.1$, well above that provided by electron captures (Gupta et al. (2007) and HZ08). Moreover, it must be released at a density $\lesssim 3 \times 10^{10}\,\mathrm{gr\,cm^{-1}}$, which is again below the density range of electron captures or other known reactions in the outer crust (like ^{24}O burning, Horowitz et al. (2008)).

We note that the steep fall in the inverted temperature gradient of the initial thermal profile is necessary to account for the relatively high temperature of the first observation ($T \simeq 120$ eV at 40 days) followed by the moderate value of the second one ($T \simeq 90$ eV at 300 days), see Fig. 9 and Fig. 10. Our results show that this profile is indeed difficult to achieve unless an extra heating source is assumed to be coming from a low density layer. It could be either from the heated up envelope during outburst (that modifies the boundary condition for the cooling through the value of T_b^0) or from the heat released by shallow sources in the outer crust. This fact was implicitly assumed in BC09 when $T_{b,8}^0$ was fixed to a relatively high value $\simeq 1$. Alternatively, it has been proposed that MXB 1659−29 has been accreting

[5] In Fig. 8 we set $T_{b,8}^{out} = 4.1$, $T_{c,8} = 0.29$, $\dot{M}_{18} = 0.1$, $Q_{imp} = 4$ and $M = 1.6\ \mathrm{M}_\odot$, similar to those used in BC09, see App. A.

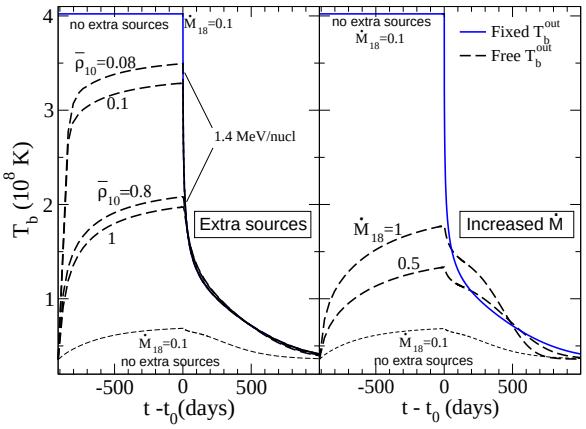

Fig. 9. Evolution of $T_{\rm b}$ when $T_{\rm b}^{\rm out}$ evolves free (dashed lines). Left panel: curves have extra heat sources at $\bar{\rho}_{10} = 0.8, 1$ ($Q_{\rm imp} = 3.5, 3.3$) and at $\bar{\rho}_{10} = 0.08, 0.1$ ($Q_{\rm imp} = 4$) with an intensity of 1.4 MeV nuc^{-1}. Right panel: curves have increasing $\dot{M}_{18} = 0.1, 0.5, 1$, ($Q_{\rm imp} = 4, 2, 0.4$). Solid lines are $T_{\rm b}^{\rm out} = 4.1$ fixed and no additional sources ($Q_{\rm imp} = 4$ and $\dot{M}_{18} = 0.1$); in all cases $T_{\rm c,8} = 0.29$.

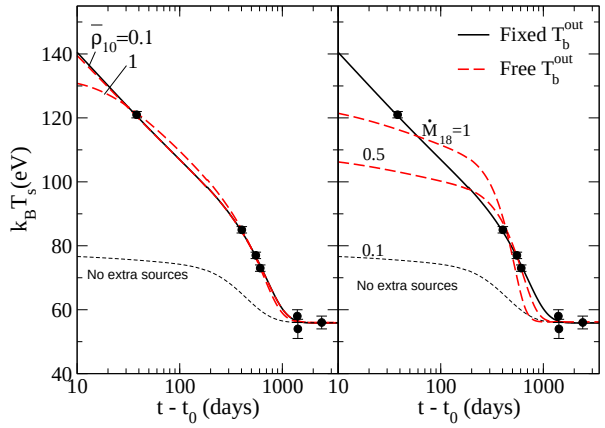

Fig. 10. Comparison of cooling curves for MXB 1659−29 with free and fixed $T_{\rm b}^{\rm out}$. Solid curve has fixed $T_{\rm b,8}^{\rm out} = 4.1$ and $Q_{\rm imp} = 4$. Dashed curves in left panel consider free $T_{\rm b}^{\rm out}$ with an extra heat source at $\bar{\rho}_{10} = 0.1, 1$ where $Q_{\rm imp} = 4, 3.3$ and $Q_{\rm add} = 1.4$ MeV nuc^{-1} . In right panel, the accretion rate is increased to $\dot{M}_{18} = 0.5, 1$ ($Q_{\rm imp} = 2, 0.4$). For all $\dot{M}_{18} \sim 0.1$ and $T_{\rm c,8} \sim 0.29$ are fixed.

at the Eddington rate $\dot{M}_{18} \sim 1$, overestimating $\dot{M}_{\rm obs}$ for MXB 1659−29 by about one order of magnitude (BC09 and Sht07).

We now study the two possibilities: shallow sources in the outer crust or increased accretion rates. In the first case we consider the location of additional sources to vary in the range $\bar{\rho}_{10} \sim (0.1-1)$ (where ρ_{10} is ρ in 10^{10} g cm^{-3}) with radial width $\Delta r = 10$ m, an energy released of 1.4 MeV nuc^{-1}, and $\dot{M}_{18} = 0.1$ (left panel of Fig. 9). Alternatively, we increase $\dot{M}$ from $\dot{M}_{18} = 0.1$ up to $\dot{M}_{18} = 1$ (right panel of Fig. 9). In both cases we find that the envelope is heated up respect to the free evolution case with no extra sources and $\dot{M}_{18} = 0.1$ (dashed line at the bottom), but $T_{\rm b}^0$ hardly reproduces the initial steep fall of a fixed $T_{\rm b}^{\rm out}$ (solid line) unless an extra shallow intense source is considered at densities $\rho_{10} \lesssim 0.08$ and with an energy released of at least 1.4 MeV nuc^{-1}.

On the other hand, the slope produced by the increased $\dot{M}$ cannot explain MXB 1659−29 early data (as shown in Fig. 10), confirming BC09 results. If the heat source is located at more external layers, $\bar{\rho}_{10} \lesssim 0.01$, then its intensity could be reduced and results are much similar to the case with $T_{\rm b}^{\rm out}$ fixed. Thus, we consider the last scenario as a limiting case of a source located at lower densities in the outer crust or even in the envelope.

We conclude that deep crustal heating by pycnonuclear reactions in the inner crust and e-captures in the outer crust is not enough to explain the early slope of MXB 1659−29 and extra energy coming from low density regions is needed. It might be from the heated up envelope during outburst or from additional shallow sources in the outer crust; to disentangle between these two options, observations shortly after accretion stop are crucial.

7. Influence of accretion: the relation $T_{\rm b}(\dot{M})$

The dependence of $T_{\rm b}$ on $\dot{M}$ presented in Sec. 5.2 provides a twofold improvement in the description of crustal cooling models. First, it accounts in a consistent way for the influence of the accretion rate and second, it reduces the number of free parameters. Moreover, we expect that by means of these relations we can set constraints on the envelope composition since they depend on the envelope model considered.

In the next subsections we analyze MXB 1659−29 and EXO 0748−676, for which we build a starting model assuming fixed $M = 1.6$ M$_\odot$ and envelope compositions PA$_{15}^{\rm deep}$ and PA$_{30}^{\rm deep}$, respectively. We leave $\dot{M}$ and $T_{\rm c,8}$ as the only free parameters, set in each case to fit the first and the last observation of each source.

MXB 1659−29

Using the $T_{\rm b}(\dot{M})$ relations we can successfully explain the high temperature of early data as a consequence of the accretion mass rate. We obtain a thermal evolution that is compatible with a low $Q_{\rm imp}$ value in the crust and we find that the source reaches thermal equilibrium in ~ 1000 days, which is in fully agreement with BC09 simulations and exponential fits in Cackett et al. (2008). Cooling curves fitting well the observations (brown regions with $\chi^2 < 2$) are shown in Fig. 11, for which we find $T_{\rm c,8} = 0.26 - 0.30$ and $\dot{M}_{18} = 0.13 - 0.15$, values included within the observational range $\dot{M}_{\rm obs,18} = 0.07 - 0.18$ (Tab. 2) . The solid curve is the best fit with $T_{\rm c,8} = 0.28$ and $\dot{M}_{18} = 0.14$ and is indicated as a cross in the inset. We choose $Q_{\rm imp} = 4$ and the envelope model PA$_{15}^{\rm deep}$ because it gives a similar core temperature as in BC09 and facilitates comparison ($T_{\rm c,8} \sim 3.5$, see App.A). If we vary the envelope model we obtain good agreement as well, this will be explored in the next Section.

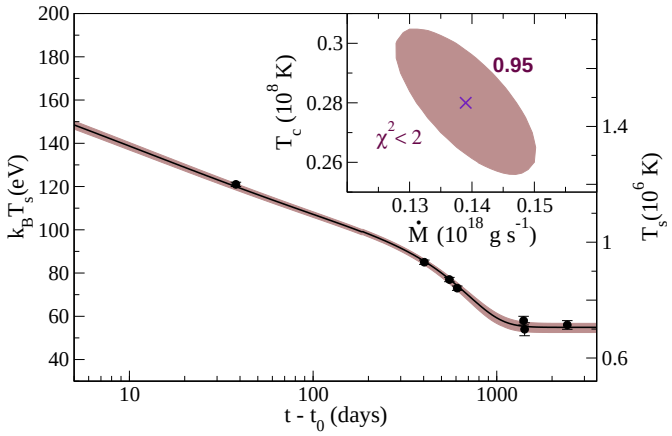

Fig. 11. Fits for MXB 1659−29 taking $T_b(\dot{M})$ relations into account. The brown zone corresponds to cooling curves with $\chi^2 < 2$. Solid line is our best fit. The inset shows the parameter space corresponding to $\chi^2 < 2$ and the cross, the minimum $\chi^2 = 0.95$. We fix PA_{15}^{deep} envelope, $M = 1.6$ M$_\odot$ and $Q_{imp} = 4$.

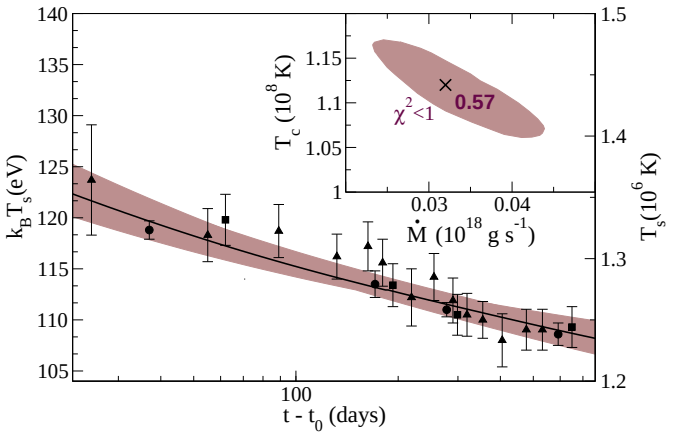

Fig. 12. Same as Fig. 11 but for EXO 0748−676. Here, brown zones are $\chi^2 < 1$ and the minimum is $\chi^2 = 0.57$. We fix PA_{30} envelope, $M = 1.6$ M$_\odot$ and $Q_{imp} = 1$.

EXO 0748−676

This source presents some characteristics that differ from MXB 1659−29 or KS 1731−260. Its quiescent luminosity is higher than the prediction by standard cooling models (Degenaar et al. 2011b). It has been suggested that the presence of residual accretion outside the main accretion period may be responsible for the high temperature (Brown et al. (1998), Rutledge et al. (2000), Colpi et al. (2001)). Nevertheless, this option seems unlikely since *XMM-Newton* telescope (which has provided the most sensitive observations) has not shown dips in the light curve, which would evidence the presence of residual accretion (Díaz Trigo et al. 2011). Alternatively, they suggested that the core has reached a steady state in which the energy radiated during quiescence equals the heat released by the reactions taking place during outburst. Considering an accretion time of 24 yrs and an accretion rate of $\dot{M}_{18} = 0.03$, a steady state with such high temperature would be compatible with a recurrence time of ∼100 yrs (Degenaar et al. 2011b), a scenario that cannot be ruled out.

Another peculiarity of this source is the small temperature decrease after outburst: the surface temperature has decreased to a factor of ∼ 0.9 in 650 days, in comparison to ∼0.5 for MXB 1659−29 in the same time period. This is again compatible with a high core temperature and a low accretion rate. Another open issue is the unknown origin of the power law component in the spectra.

In spite of such peculiarities, EXO 0748−676 quiescent luminosity can also be very well explained trough $T_b(\dot{M})$ relations. Our fits indicate that the source will level off at $k_B T_s \sim 105$ eV in $t \sim 4000$ days (Fig. 12), which is compatible with observational exponential fits which predict $k_B T_s \sim 107$ eV. Indeed, the core temperature is high, $T_{c,8}$ ∼1, one order of magnitude higher than in MXB 1659−29 case, which might evidence that EXO 0748−676 is a young NS which core has not yet reached thermal equilibrium. The envelope model used here is PA_{30}^{deep} and the impurity parameter fixed to $Q_{imp} = 1$; given that the source is hot, it is quite insensitive to variations of Q_{imp}. Free parameters vary in the ranges $T_{c,8} = 1.07-1.17$ and $\dot{M}_{18} = 0.02-0.035$, well close to the observational rate $\dot{M}_{obs,18} = 0.03$. Note that brown regions denote very good fits with $\chi^2 < 1$; the best one corresponds to $T_{c,8} = 1.12$ and $\dot{M}_{18} = 0.027$.

It is important to note that it seems to be a shift between the *Chandra* and *Swift* observations which is maybe due to cross-calibration issues between the two satellites (Degenaar et al. 2011b). Even more, *XMM-Newton* and *Swift* fluxes are compatible, which also points to an offset in the calibration between *Chandra* and *Swift* (Díaz Trigo et al. 2011). Due to the small error bars *Chandra* data allow for a better constraint of $\dot{M}$ and T_b, but these data do not provide information of early times. Conversely, *Swift* data allow for a better description of the early time and *XMM-Newton* data are the most sensitive observations of this source in quiescence and, therefore, the most reliable (Díaz Trigo et al. 2011). We first fitted *XMM-Newton* and *Swift* data together to find $T_{c,8} = 1.10$, while *Chandra* data gives $T_{c,8} = 1.12$. Given this tiny difference, we decided to include all available data in the following analysis.

8. Dependence on the envelope composition

The results presented so far (Figs. 11 and 12) depend on the envelope models. Now we explore the sensitivity of the inferred values of T_c and $\dot{M}$ to variations in the envelope composition for the cases of MXB 1659−29, KS 1731−260 and EXO 0748−676.

In Figs. 13 we show contour plots in the T_c - $\dot{M}$ parameter space, defined by the condition $\chi^2 < 2$. We show results for different envelope models in which we vary the density at which light elements occurs (FA, PA models) as well as the H-content within a model (percentage close to each ellipse). We contrast our results with the observational

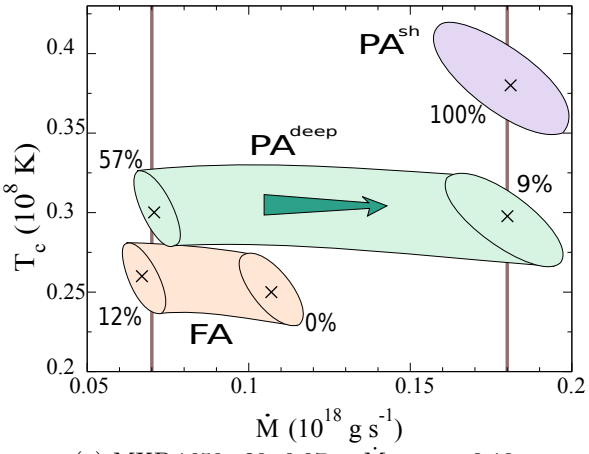

(a) MXB 1659−29; $0.07 < \dot{M}_{\rm obs,18} < 0.18$

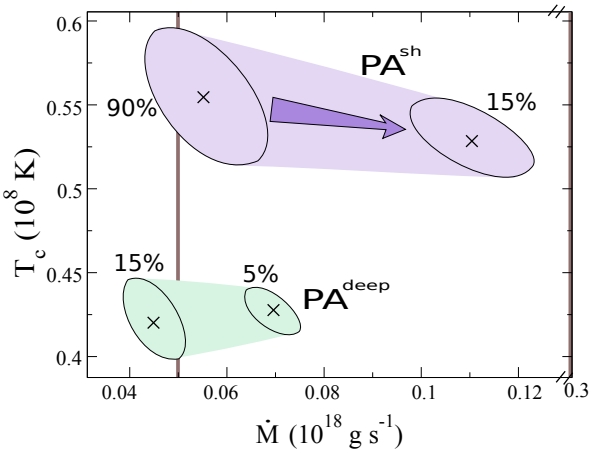

(b) KS 1731−260; $0.05 < \dot{M}_{\rm obs,18} < 0.3$

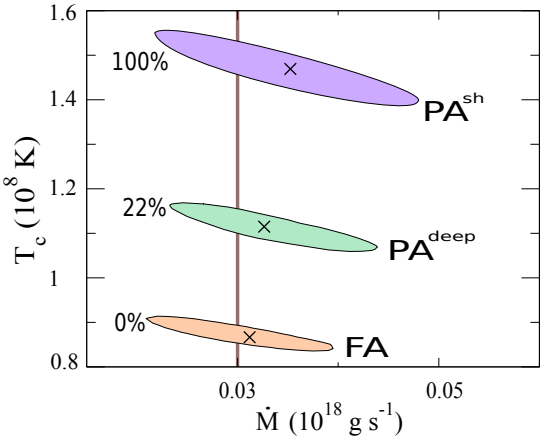

(c) EXO 0748−676; $\dot{M}_{\rm obs,18} \sim 0.03$

Fig. 13. Contours for $\chi^2 < 2$ for three sources varying the envelope compositions. In each panel the corresponding range for the observational accretion rate is shown as vertical lines. The H percentage is denoted in each case close to the contours.

limits for $\dot{M}$, marked with vertical lines. In all the cases, a 1.6 $M_\odot$ NS star with a low value of $Q_{\rm imp}(\lesssim 10)$ is chosen.

We observe that, in envelopes with a low hydrogen content, nuclear reactions release less energy and $T_{\rm b}^0$ reaches lower values. For example we obtain $T_{\rm b,8}^0 \sim 2$ for $\dot{M}_{18} = 0.1$ when we consider $\mathrm{PA}_0^{\rm deep}$ model, and $T_{\rm b,8}^0 \sim 5$ when we consider $\mathrm{PA}_{50}^{\rm deep}$ model (see Fig. 7). Therefore, $\dot{M}$ needs to be increased and the contours shift toward the region of higher accretion rates (shown by arrows in Figs. 13a and 13b). In this way, looking for contours which minimums are close to the $\dot{M}$ observational limits, we can set constraints on the envelope composition.

For MXB 1659−29 we find that if one assumes that the envelope is only marginally modified by the accretion and light elements reach only shallow depths ($\mathrm{PA}^{\rm sh}$), only H must be present in the light-elements shell and practically no He-content (Fig. 13a). Conversely, for strong accreted envelopes in which heavy elements only occur at higher densities ($\mathrm{PA}^{\rm deep}$), He must be present in that shell in at least $\simeq 40\%$ and may increase up to 100% in fully accreted ones (FA).

We find qualitatively similar results for KS 1731−260 (Fig. 13b), but in this case the imprint of He seems to be even stronger. The main difference may be that data cannot be fit with fully accreted scenarios (no solution with FA model is found). If $\mathrm{PA}^{\rm deep}$ models are considered, the required He content is even larger than for MXB 1659−29 with values of 85-95%. Nevertheless some H seems to be necessary to explain the data. On the other hand, considering $\mathrm{PA}^{\rm sh}$ models, the H content may increase up to 90%, as for the previous source. Finally, we show results for EXO 0748−676 (Fig. 13c) that confirm the tendency obtained so far. Note that in this case $\dot{M}$ is constrained by a single value instead of a range, allowing for a much better determination of the envelope type. Again, marginally partial accreted envelopes ($\mathrm{PA}^{\rm sh}$) require full H-content, strong partially accreted envelopes ($\mathrm{PA}^{\rm deep}$) a rather high level of He-content $\simeq 80\%$, and fully accreted ones admit only He.

We conclude from this analysis that when one moves from marginally accreted envelopes to fully accreted envelopes, the H-content necessary to explain the observations decreases accordingly. This trend is also modulated with the observational mass accretion rate, the lower the rate the higher the H-content. Therefore, a better determination of the mass accretion rate is crucial to determine the envelope composition more precisely.

9. Towards a canonical model for crustal coolers: constraining the crust microphysics

This section is devoted to infer some information about the crust microphysics. We focus mainly on new constraints imposed by the last observation of KS 1731−260 and on trying to find a *canonical model* that fits simultaneously the quiescence emission of MXB 1659−29, KS 1731−260, and EXO 0748−676.

9.1. Is KS 1731−260 still cooling? Constraints on neutron superfluidity energy gaps

Last observations of KS 1731−260 reported by Cackett et al. (2010a) seem to indicate that the source is still cooling and that previous models fail to explain the last data point (Fig. 1b). A longer relaxation time with a larger storage of heat in the crust is needed. For our current set of microphysical inputs, none of the curves obtained varying $Q_{\rm imp}$, $T_{\rm c}$ or $\dot{M}$ succeed in explaining the temperature of the last observation. To obtain cooling curves with longer crustal relaxation times (compared to

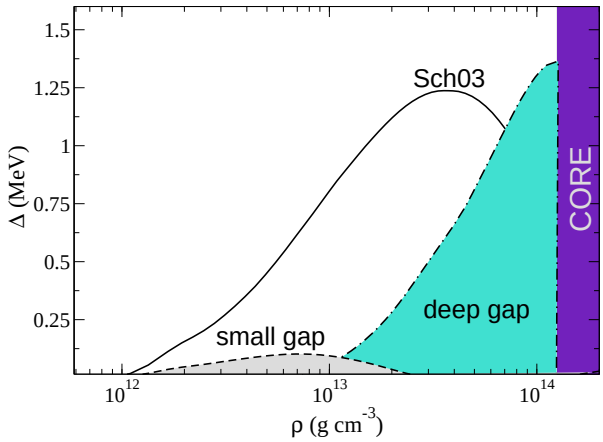

Fig. 14. Energy gap models as function of density, Schwenk et al. 2003 gap (Sch03, solid line), *deep* gap (dashed dotted line) and *small* gap (dashed line).

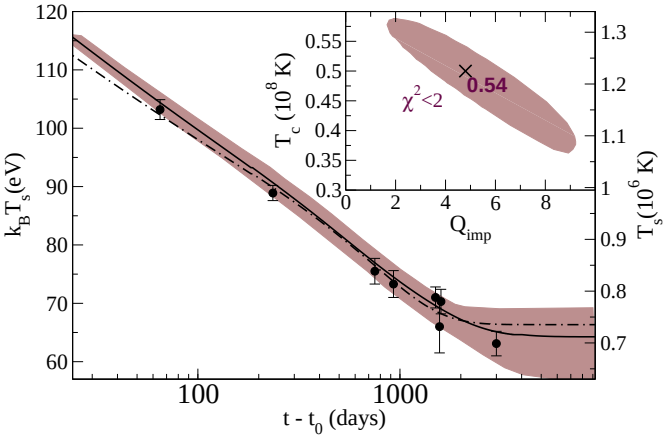

Fig. 15. Cooling curves for KS 1731−260 using a "deep" gap: the brown zone corresponds to $\chi^2 < 2$ and the solid curve is the best fit ($\chi^2 = 0.54$) with $\mathrm{PA}^{\mathrm{sh}}_{100}$ envelope. Dotted-dashed curve corresponds to the best fit ($\chi^2 = 1.08$) with the Sch03 gap and $\mathrm{PA}^{\mathrm{sh}}_{90}$. In all cases $M = 1.6\ \mathrm{M}_\odot$ and $\dot{M}_{18} = 0.05$ are fixed.

MXB 1659−29) we explore the possibility of a neutron energy gap for superfluidity with a relatively low maximum value (hereafter *small* gap), or, alternatively, located at deep densities (hereafter *deep* gap) such that the resulting suppression of the neutron specific heat is less efficient.

In Fig. 14, we show different functional forms for the density dependence of the neutron superfluidity energy gaps. Up to now, we have been using the fit Schwenk et al. (2003) (Sch03) which is similar to the model used in BC09 or SHT07. Its influence extends in the range $\rho \sim (10^{12} - 10^{14})\,\mathrm{g\,cm^{-3}}$ with a maximum value of $\simeq$ 1MeV. Below this temperature, the specific heat is strongly suppressed respect to the non-superfluid case. The model called *deep* gap (dashed dotted line in Fig. 14) has a maximum located near the crust-core interface, at $\rho \sim 10^{14}\,\mathrm{g\,cm^{-3}}$, that leads to a less efficient suppression to the specific heat in most of the crust with a consequent increase of the thermal relaxation time. A similar effect can be obtained if we consider a *small* gap with maximum value about $\simeq$ 0.1MeV, one order of magnitude smaller than Sch03 (dashed line).

The Sch03 gap fails to fit observations as shown by the best fitting cooling curve obtained (dotted-dashed line in Fig. 15). Due to the longer relaxation time, cooling curves using a deep gap can fit substantially better the last observation of KS 1731−260. Moreover, we checked that data can be fitted as well if we do not consider suppression at all. This means that any gap contained within the colored regions bellow deep and small gaps in Fig. 14 can provide a good fit. Obviously, a lower $T_{\mathrm{c},8} \simeq 0.5$ is reached in this new fit, which indicates that indeed the source is still cooling.

9.2. Constraining the impurity parameter

In this subsection we explore the $Q_{\mathrm{imp}}-T_{\mathrm{c}}$ parameter space for the three sources: MXB 1659−29, KS 1731−260, and EXO 0748−676.

In the top panels of Fig. 16 and Fig. 17 we show contour levels corresponding to cooling curves that satisfy the conditions $\chi^2 < 2$ (light regions) and $\chi^2 < 1$ (dark regions), obtained for the Sch03 gap and two different masses, $M = 1.4\ \mathrm{M}_\odot$ (left panels) and $M = 1.6\ \mathrm{M}_\odot$ (right panels). In bottom panels, we show equivalent results for a deep gap. In the different panels we also vary the mass accretion rate $\dot{M}$ within the observational range as much as possible; the ellipses with solid (dashed) contours are calculated for the upper (lower) limit and the ones with dotted lines correspond to intermediate values.

First we can note some general trends in the figures:
i) Q_{imp} is correlated with $\dot{M}$; as $\dot{M}$ is increased, the energy released in the inner crust by pycnonuclear reactions is increased, overheating the deep layers. To balance this effect, Q_{imp} must assume a lower value, which raises the thermal conductivity favoring heat transport to the core.
ii) a more massive NS has a thinner crust which reduces the thermal relaxation time and Q_{imp} suffers a shift toward higher values.
iii) T_{c} varies with the envelope model used; its value is increased as ρ_{h} decreases (the density at which heavy elements occur) since the opacity of the envelope is higher and the interior temperature needs to be high in order to keep T_{s} in the value required by observations.

In particular for KS 1731−260 (Fig. 16), we find that considering the Sch03 energy gap it is not possible to fit the data with parameters that satisfy $\chi^2 \lesssim 1$, even varying the NS mass. However, taking the deep energy gap the data can be well fitted ($\chi^2 \lesssim 1$) with $Q_{\mathrm{imp}} \sim 4-8$ (for both masses), and $T_{\mathrm{c},8} \sim 0.3-0.5$ ($T_{\mathrm{c},8} \sim 0.4-0.6$) for $M = 1.4\ \mathrm{M}_\odot$ ($M = 1.6\ \mathrm{M}_\odot$).

In contrast, fits for MXB 1659−29 (Fig. 17) show that both gaps can fit the data. Choosing the Sch03 energy gap we obtain $Q_{\mathrm{imp}} \sim 1-3$, and $T_{\mathrm{c},8} \sim 0.3-0.4$ for $M = 1.4\ \mathrm{M}_\odot$. Alternatively, considering the deep energy gap with $\chi^2 < 1$ we find $Q_{\mathrm{imp}} = 1.4-2.4$ and $T_{\mathrm{c},8} = 0.25-0.29$, being $M = 1.4\ \mathrm{M}_\odot$ and $\mathrm{PA}^{\mathrm{deep}}$ fixed.

We turn now to compare these results with EXO 0748−676 (see Fig. 18). Since the last observation of this source was detected at $\sim$ 600 days, and the

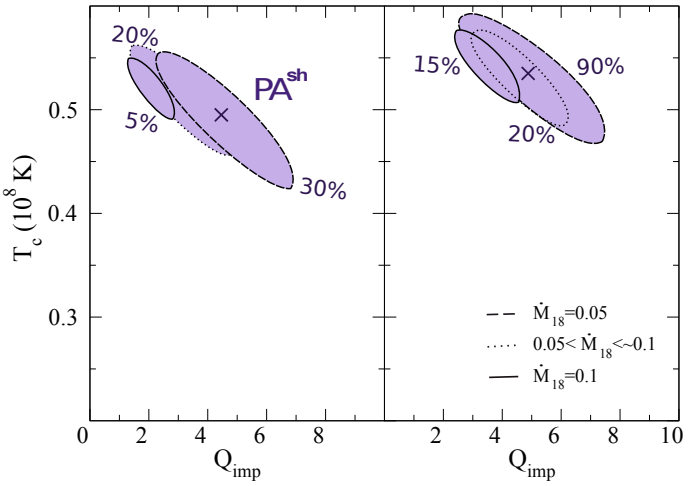

(a) Sch03 gap. $M = 1.4$ M$_\odot$ (left), $M = 1.6$ M$_\odot$ (right).

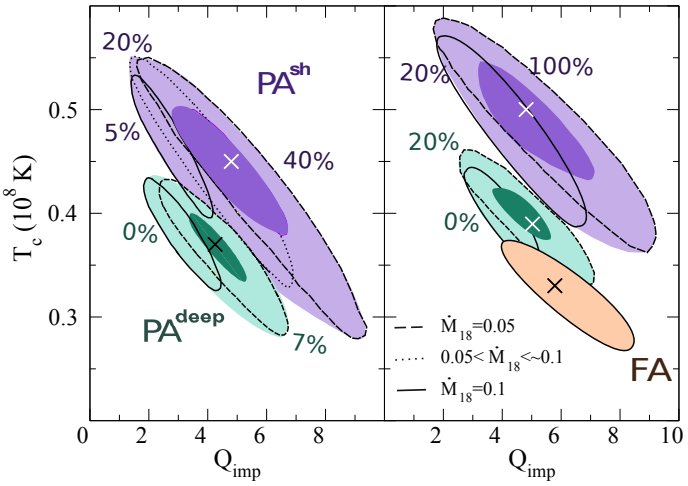

(b) Deep gap. $M = 1.4$ M$_\odot$ (left), $M = 1.6$ M$_\odot$ (right).

Fig. 16. Contours for KS 1731−260 source satisfying $\chi^2 < 1$ (dark regions) and $\chi^2 < 2$ (light regions) considering different envelope compositions, energy pairing gaps, NS masses and mass accretion rates.

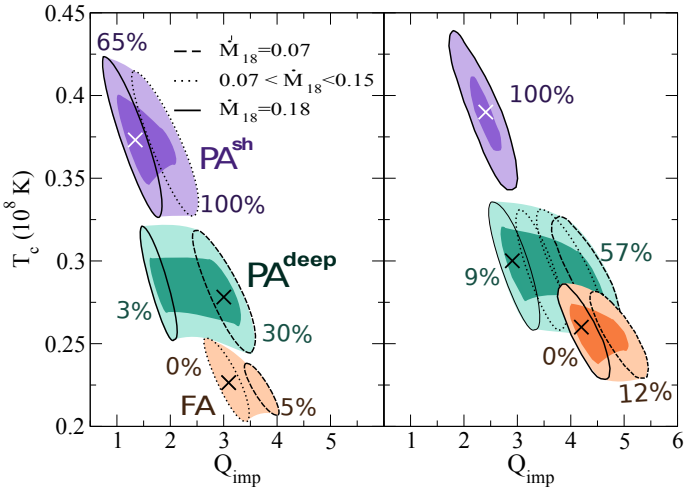

(a) Sch03 gap. $M = 1.4$ M$_\odot$ (left), $M = 1.6$ M$_\odot$ (right).

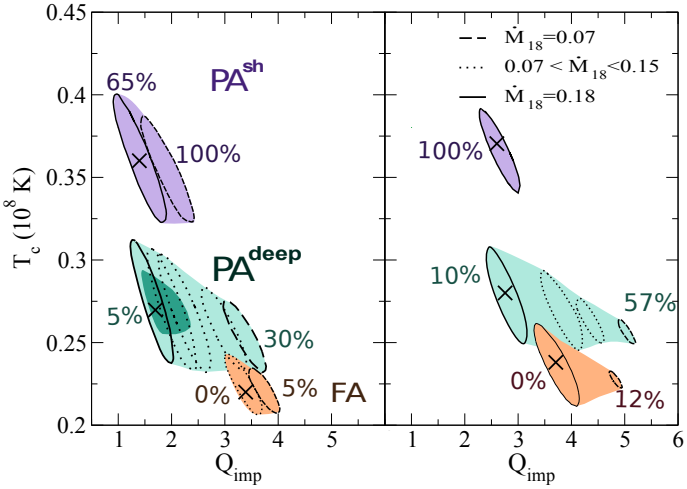

(b) Deep gap. $M = 1.4$ M$_\odot$ (left), $M = 1.6$ M$_\odot$ (right).

Fig. 17. Contours for MXB 1659−29 source satisfying $\chi^2 < 1$ (dark regions) and $\chi^2 < 2$ (light regions) considering different envelope compositions, energy pairing gaps and NS masses.

energy gap influences cooling curves only after ~ 500 days, it is too early to distinguish between models. Considering either Sch03 or a deep gap does not make a significant difference. The allowed range of parameters is much wider than for the other two cases.

It is worth noticing that, because at high temperatures ($T \gtrsim 10^8$ K) the contribution to the thermal conductivity due to e-impurities scattering is negligible, cooling curves are barely dependent on $Q_{\rm imp}$. On the other hand, when we consider the FA model, lower values for $T_{\rm c}$ are allowed to fit data and the contribution due to $Q_{\rm imp}$ becomes important. In this case, high values of $Q_{\rm imp}$ fit the data balancing the fast cooling due to a low $T_{\rm c}$. In the high $T_{\rm c}$ case, $Q_{\rm imp}$ can reach high values because of the weak dependence of cooling curves on this parameter, instead, for low $T_{\rm c}$, $Q_{\rm imp}$ must reach high values to compensate.

Comparing results for MXB 1659−29, KS 1731−260 and EXO 0748−676 sources (summarized in Tab. 6), we note that while EXO 0748−676 shows a higher equilibrium core temperature, $T_{\rm c,8} \sim 1$, MXB 1659−29 and KS 1731−260 seem to level off at $T_{\rm c,8} \sim$0.3-0.4. We stress that for the three sources we obtain good fits ($\chi < 1$) with corresponding mass accretion rates compatible with those inferred from observations. Therefore, a *canonical* model that fits the three sources simultaneously points to the following characteristics:

1. the NS mass is rather low ($M \simeq 1.4 M_\odot$),
2. the favored envelope model requires the appearance of heavy elements at $\rho_h \simeq 0.3\rho_8$, like PA$^{\rm deep}$,
3. the light elements shell consist mostly of He (low H-content of $x \lesssim 10\%$),
4. the energy gap for neutron superfluidity has a relatively small maximum value ($\simeq$ 0.1MeV) or it is peaked at deep densities close to the crust-core interface ($\rho \sim 10^{14}\,{\rm g\,cm^{-3}}$),
5. the impurity parameter is $Q_{\rm imp} \lesssim 5$

This allows us to call these three sources *standard crustal coolers*; despite of their differences, their quiescent emission can be explained by means of the heat released by pycnonuclear reactions deep in the inner crust, as long as NS models and microphysics are adjusted. There are in fact two other sources, XTE J1701−462 and IGR J17480−2446

Table 6. Constraints for MXB 1659−29, KS 1731−260, and EXO 0748−676 envelope model, H fraction X, core temperature T_c and mass accretion rate $\dot{M}$, considering a *deep* gap (impurity parameter varying in the range $Q_{\rm imp} = 0 - 5$). Rows highlighted in grey correspond to a *canonical* model that fits the three sources simultaneously.

Source	Mass	Envelope model	X	$T_{c,8}$ (K)	$\dot{M}_{18}$	$\chi^2_{\rm min}$
MXB 1659−29	1.4	PA$^{\rm deep}$	3-30%	$0.27^{\pm 0.02}$	0.18	0.68
KS 1731−260	1.4	PA$^{\rm sh}$	5-40%	$0.45^{+0.04}_{-0.09}$	0.05	0.66
		PA$^{\rm deep}$	0-7%	$0.37^{+0.03}_{-0.04}$	0.05	0.76
	1.6	PA$^{\rm sh}$	20-100%	$0.50^{+0.05}_{-0.07}$	0.05	0.54
		PA$^{\rm deep}$	0-22%	$0.39^{+0.03}_{-0.02}$	0.05	0.79
EXO 0748−676	1.4	PA$^{\rm deep}$	12%	$1.07^{+0.04}_{-0.07}$	0.030	0.58
		PA$^{\rm sh}$	100%	$1.47^{\pm 0.09}$	0.034	0.60
	1.6	PA$^{\rm deep}$	22%	$1.12^{\pm 0.04}$	0.032	0.63
		FA	3%	$0.87^{\pm 0.04}$	0.031	0.56
	1.8	PA$^{\rm deep}$	60%	$1.19^{+0.05}_{-0.04}$	0.029	0.59

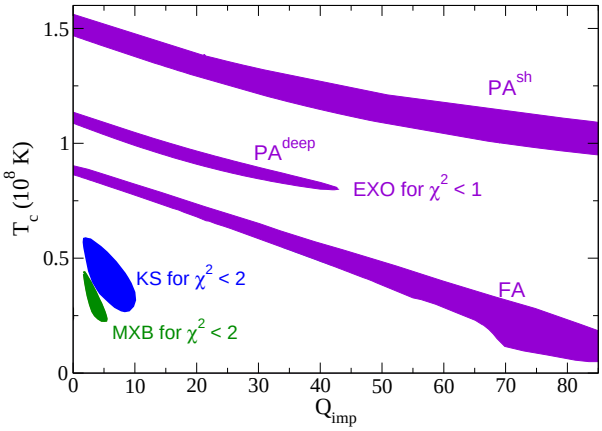

Fig. 18. Contours for EXO 0748−676 source satisfying $\chi^2 < 1$ and different envelope compositions. We also show the approximate parameter space defined by MXB 1659−29 and KS 1731−260 contours.

for which this assumption is not sufficient to account for their quiescent emission and additional heat sources in the outer crust/envelope, residual accretion or new processes affecting the thermal conductivity of the crust, have to be assumed as we discuss next.

10. Beyond crustal cooling

The peculiar observational data of XTE J1701−462 and IGR J17480−2446 require models that include additional considerations beyond the deep crustal cooling model controlled by pycnonuclear reactions an electron captures in the inner crust. In this Section we investigate scenarios that could help to understand the quiescent emission for these warm sources: an extra heat deposition in the outer crust via additional sources, a modified heat flow due to a buried magnetic field or residual accretion as responsible for the increment/variability in the temperature.

10.1. Extra heat in the outer crust?

First we study the possibility of extra heat sources located in the outer crust that could modify the initial thermal profile for the cooling. Gupta et al. (2007) calculated the heat released for all thermonuclear reactions in the outer crust assuming a one-component plasma and found ∼0.2 MeV nuc^{-1}. Later, Horowitz et al. (2008) calculated reaction rates of ^{24}O and ^{28}Ne for a multicomponent plasma and found that a composition in which $(3 - 10)\%$ of the ions are ^{24}O, gives place to reactions which release 0.52 MeV nuc^{-1} and occur at a density of $\sim 10^{11}$ g cm^{-3}. This energy could indeed influence the thermal state of the source going into quiescence.

Since the crustal cooling timescale depends on the initial thermal profile, if this is peaked in the outer crust (typically 10^8-10^9 gr cm^{-3}, see Fig. 19), it may give a plausible explanation for the break observed at $\sim 20 - 150$ days in XTE J1701−462 (Fig. 2d). Additional heat sources located in the outer crust releasing large enough energy per nucleon could account for such kind of initial profiles (Fridriksson et al. (2010), BC09, Degenaar & Wijnands (2011a)).

XTE J1701−462

This is the most peculiar source: in two observations, XMM-3 and CXO-4, it shows a sudden increase in the temperature which lacks of explanation so far. Ignoring these two observations, the exponential fit gives the shortest e-folding time ∼ 100 days and the broken power law fit predicts a break in the slope around ∼25–80 days (Fridriksson et al. 2011) (much earlier than the other sources). BC09 suggested that the break is due to the suppression of the specific heat in the transition from a classical to a quantum crystal. They estimated the time at which the break occurs (the diffusion time of the thermal flow from the density at which this

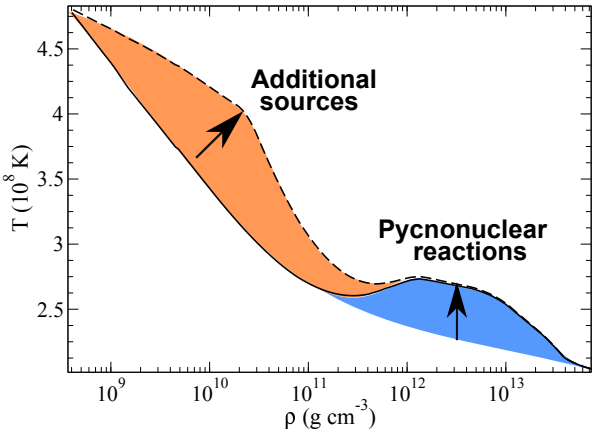

Fig. 19. Heat sources influence on the initial thermal profile.

transition occurs to the surface) and obtained ~ 300 days, much larger than expected from the data.

It is also difficult to reconcile the early temperature of XTE J1701−462 with the latest observations within a cooling model. More specifically, we can easily find a set of parameters for the thermal evolution that explains the first observation at the third day (COX-1) and the tail after ~ 400 days (COX-5 and subsequent), but the problem is to fit the data between ~ 10 and ~ 200 days with the same model.

An alternative explanation for the fast initial drop in the temperature is the presence of extra heat sources in the outer crust that release energy close enough to the surface for the heat to be rapidly carried away. After this first stage, the temperature evolution should resemble the standard cooling model without extra heat sources. If this is the case, the early data of XTE J1701−462 are unique and offer valuable information about the depth of the layer where additional heat is released. The initial thermal profile is modified by the location of heat sources; if we consider shallow sources ($\bar{\rho}_{10} \lesssim 10$) the heat accumulated during the accretion stage diffuses mostly to the surface, keeping the outer crust hot at early times. Instead, if we consider deep sources, the heat is carried towards the interior and released by neutrino emission from the core, resulting in lower surface temperatures.

We perform simulations considering that the extra heat is located in a shell characterized by the mean density, $\bar{\rho}$, at which the energy is deposited and its radial width, Δr. We fix the envelope model to $\mathrm{PA}_0^{\mathrm{sh}}$ because it gives a T_{b} value compatible with observations for an accretion rate of $M_{18} = 1.1$, and $Q_{\mathrm{imp}} = 1$ since the source is relatively hot and the contribution to the electronic thermal conductivity due to impurities is negligible. We have checked that results are not sensitive to the width Δr, as long as it varies in the range $(1 - 50)$ m. Thus, we keep $\Delta r = 20$ m fixed. Fixing T_{c}, $\dot{M}$ and Q_{imp} to fit the first observation together with all the $t > 100$ days data point, we find that the best fit to the intermediate observations gives $\bar{\rho}_{10} = 2.3$ and $q = 0.27$ MeV nuc^{-1} (solid curve in Fig. 20). If we fix T_{c} to a higher (lower) value, heat sources must be less (more) intense and located at shallow (deeper) layers. Considering that T_{c} varies in the range $T_{\mathrm{c},8} = 1.45 - 1.60$, set by the last observations, we find that the position and energy release of the heating sources are in the range $\bar{\rho}_{10} = (0.5 - 8.0)$ and $q = (0.1 - 0.4)$ MeV nuc^{-1} (see brown contour in inset satisfying $\chi^2 < 2$). Compared with Horowitz et al. (2008) calculations for the ^{24}O+^{24}O reaction[6], our simulations predict a (one order of magnitude) lower $\bar{\rho}$ for the heat deposition. Nevertheless, in that work the effect of neutron skin dynamic is not considered, which might result in a significant enhancement of the reaction rate and, hence, a lowering of $\bar{\rho}$.

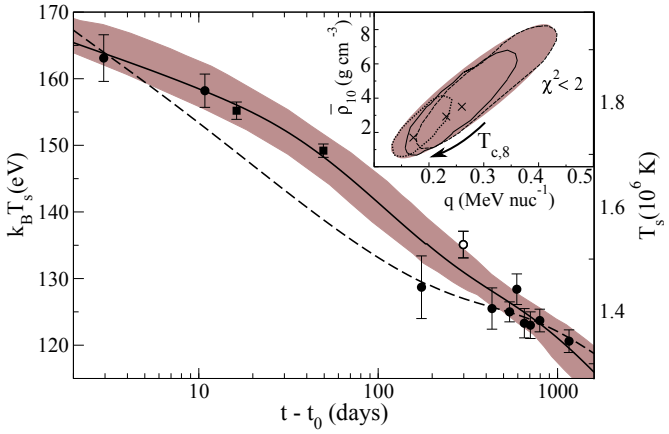

Fig. 20. Best cooling curves for XTE J1701−462 with additional heat sources optimized respect to $\bar{\rho}_{10}$ and q. Brown region and contours in the inset satisfy $\chi^2 < 2$. Contours were calculated fixing $T_{\mathrm{c},8} = 1.6, 1.5, 1.45$ (dotted, solid and dashed line) with minima at $\chi^2 = 0.87, 0.80, 084$, respectively. The dashed line is the base cooling curve in Fig. 25b without additional heat sources. We fix $T_{\mathrm{c},8} = 1.5$, $\dot{M}_{18} = 1.1$, $\Delta r = 20$ m, and $\mathrm{PA}_0^{\mathrm{sh}}$ envelope.

IGR J17480−2446

This is the first regular transient with a short active phase of $\sim$ weeks/months showing evidence of crustal cooling. It is remarkable that having been accreting for a much shorter period than the quasi-persistent sources, its thermal flux remains, after 2.2 years, still well above the quiescent emission value detected before outburst. For such a short active phase, it would be expected that the crust reaches a lower temperature.

The information on the previous quiescent equilibrium level imposes a constraint on T_{c}. If we leave T_{c} as a free parameter in our fits, we find that the NS crust will level off after ~ 2000 days at a temperature of $T_{\mathrm{c},8} = 0.67$, which is far above than the pre-burst quiescent level $\sim (0.44 - 0.55) \times 10^8$ K (see solid curve in Fig. 21), in agreement with Degenaar et al. (2013) results.

Alternatively, if we fix T_{c} to the value in the previous quiescence period, all cooling curves underestimate the late times temperatures (dashed curve in Fig. 22). One possible solution is again the presence of additional heat sources (Degenaar & Wijnands 2011a; Degenaar et al. 2011a); results are plotted in Fig. 22. Models satisfying the condition $\chi^2 < 2$ are shown as brown regions and the best fit corre-

[6] We infer $\bar{\rho}_{10} \sim 10$ and $q =\sim 0.1$ Mev nuc^{-1}, assuming that only 10% of ^{24}O was burnt.

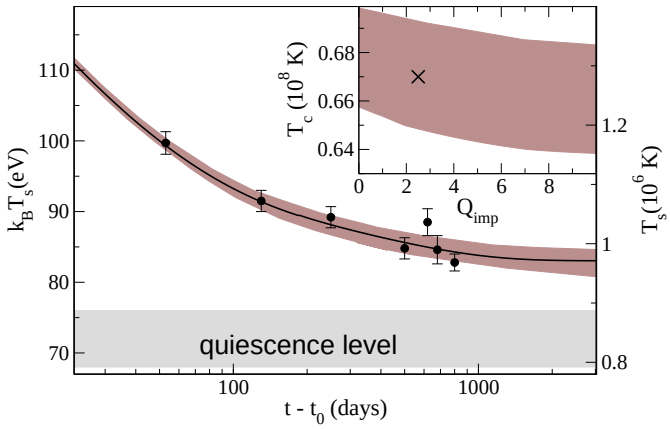

Fig. 21. Best cooling curves for IGR J17480−2446; brown zones corresponds to $\chi^2 < 2$ and the solid line (cross in the inset) is the best fit with $\chi^2 = 1.2$. We fix $\dot{M}_{18} = 0.2$, $M = 1.6$ M$_\odot$, and PA$_5^{\rm deep}$ envelope.

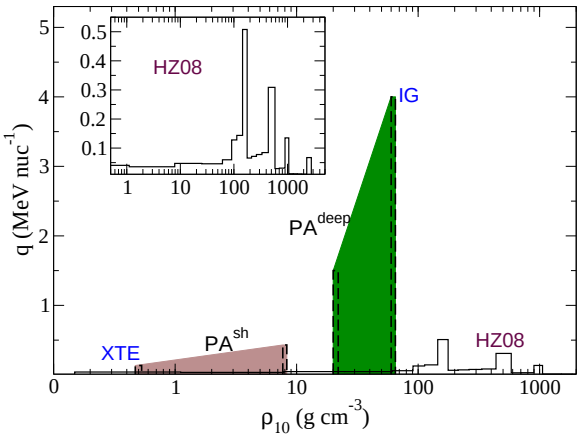

Fig. 23. Additional heat sources distribution and intensity for XTE J1701−462 (brown region, with PA$^{\rm sh}$ envelope), and IGR J17480−2446 (green region, with PA$^{\rm deep}$ envelope). Solid lines are HZ08 sources.

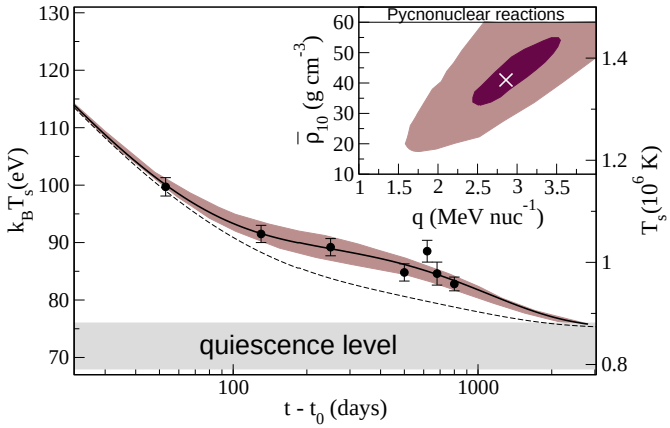

Fig. 22. Best cooling curves for IGR J17480−2446 with additional heat sources optimized respect to $\bar{\rho}_{10}$ and q. Brown region and light contours in the inset correspond to $\chi^2 < 2$, dark contours to $\chi^2 < 1$. Solid line is the minimum $\chi^2 = 0.91$ (cross in the inset) with $\bar{\rho}_{10} = 40$ and $q = 2.8$ MeV nuc^{-1}. We fix $T_{\rm c,8} = 0.55$, $\dot{M} = 0.2$ and PA$_{15}^{\rm deep}$ envelope. Dotted line is fixing T_c to the quiescent level without extra heat sources.

sponds to $q = 2.8$ MeV nuc^{-1} and $\bar{\rho}_{10} = 40$ with $\chi^2 = 0.91$ (solid curve).

Comparing these results with previously found for XTE J1701−462, we note that these heat sources are extremely intense and deep, and its origin can be hardly justified. Nevertheless, we find solutions in the parameter space delimited by the condition $1 < \chi^2 < 2$, which are compatible with shallower and less intense sources, e.g. $q \sim 1.6$ MeV nuc^{-1} and $\bar{\rho}_{10} \sim 18$ (with $\chi^2 \sim 1.9$, PA$_{15}^{\rm deep}$ and $Q_{\rm imp} = 10$).

We conclude that there are two different possibilities that can explain the observations of IGR J17480−2446. First, standard cooling (without additional heat sources) but with an equilibrium temperature well above the value measured in the previous quiescent phase. This can be a consequence of a change in the $T_{\rm b}$–$T_{\rm s}$ relation respect to the previous quiescent phase (because of a change in the envelope composition during the accretion phase) which could set a higher observed equilibrium level for the same interior temperature (Degenaar et al. 2013). Second, it is also possible to fit the data by fixing $T_{\rm c}$ in a value compatible with the quiescent band, but then it is necessary to consider very intense additional heat sources which origin is unclear. Future monitoring on IGR J17480−2446 will determine if the source has leveled off, favoring the first scenario, or it is still cooling, which would point to non standard cooling.

To summarize, in Fig. 23 we compare the additional heat sources needed for XTE J1701−462 and IGR J17480−2446 with the theoretical calculations of HZ08. Coloured bands illustrate how the source intensity is modified when they are located at different depths. The inset shows in more detail the HZ08 results.

10.2. A buried magnetic field

Another possibility that could explain a warmer outer crust at early times is the presence of a low conductivity layer between the outer and the inner crust. This can be the result of a buried magnetic field, as suggested by Payne & Melatos (2004), if during the accretion period the magnetic field lines are pushed into the crust and concentrate in a thin shell. The thermal conductivity will be highly reduced in the thin layer, and would act as a thermal insulator between the outer and the inner crust. The cooling curves will be affected by the suppressed thermal conduction resulting in an accelerated cooling at early times (released of the heat deposited in the outer crust) followed by a slower temperature decrease.

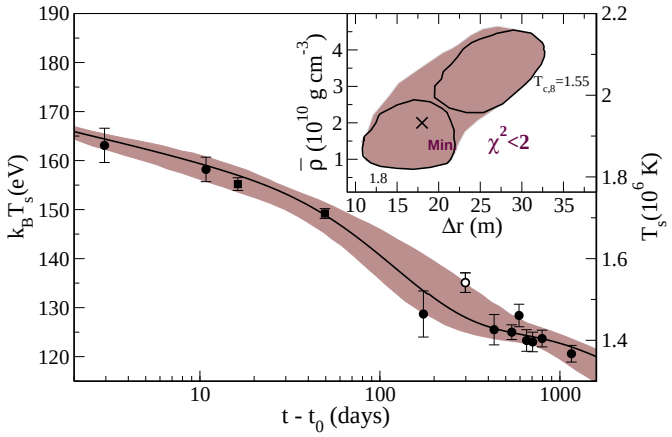

Fig. 24. Cooling curves obtained by suppressing the electron thermal conductivity by $R_{\rm sup} = 0.1$ for parameters varying in: $\bar{\rho}_{10} = 1 - 5$, $\Delta r \sim (10 - 30)\,$m and $T_{\rm c,8} = 1.55 - 1.8$. The brown band corresponds to $\chi^2 < 2$ and the solid line to $\chi^2 = 0.72$. We fixed $\dot{M}_{18} = 1.1$. Inset shows $\chi^2 < 2$ contours in parameter space varying T_c.

To test this hypothesis we suppress the electronic thermal conductivity with a factor $R_{\rm sup} = 0.1$ in a layer characterized by its radial width, Δr, and the mean density $\bar{\rho}$ at which the suppression occurs, fixing the accretion rate to the observational value, $\dot{M}_{18} = 1.1$. Results show that the parameter range compatible with the observations is $\bar{\rho}_{10} = (1. - 5.)$ and $\Delta r = (10 - 30)\,$m (Fig. 24), with a minimum at $\bar{\rho}_{10} = 1.2$ and $\Delta r = 17\,$m (with $\chi^2 < 1$). In order to make a more exhaustive analysis it is necessary to study the magnetic field geometry influence on the results in a 2D-model.

10.3. Residual accretion in XTE J1701−462?

As an alternative scenario, we speculate that some data points in the emission of XTE J1701−462 may exhibit an increased temperature due to residual accretion episodes respect to a *baseline* standard cooling. The neutron star mass is fixed to $M = 1.6\ {\rm M}_\odot$ and the envelope model to ${\rm PA}_{10}^{\rm sh}$. The best cooling curves are obtained considering the accretion rate $\dot{M}$ and the core temperature $T_{\rm c}$ as free parameters.

Then we add two residual accretion periods: in the first $\sim$ 150 days the period A coincident with CXO-2, XMM-1 and XMM2 and later, at about 200 days, with a duration of $\sim$ 60 days, the period B in correlation with XMM-3 and CXO-4. We model the accretion mass rate with an exponential decay $\dot{M}_{A,B}(t) = \dot{M}_0 e^{-(t-t_{A,B})/\mu}$ with $\dot{M}_0 = 0.35 \times 10^{18}\,{\rm g\,s^{-1}}$, $\mu = 102$ days, $t_A = t_0$ and $t_B = 215$ days for the accretion periods A and B, respectively. The functional form of $\dot{M}_{A,B}$ and the temperature at the base of the envelope $T_{\rm b}$ for the periods A and B are shown in Fig. 25a with dashed-dotted and dotted lines, respectively.

Cooling curves with residual accretion included are shown in Fig. 25b. The brown region demarcates the curves that fit filled points with $\chi^2 < 1$. The solid line is the best

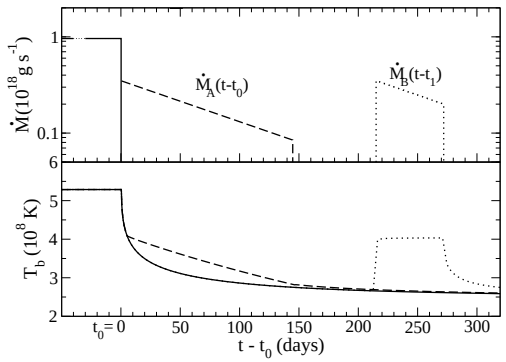

(a)

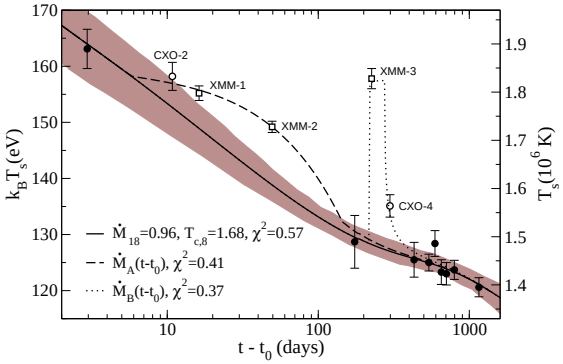

(b)

Fig. 25. Upper panel: Accreted mass rate during outburst $\dot{M} \equiv 0.96$ (solid line) and during quiescence $\dot{M}_{A,B}(t)$ (dashed and dotted lines, respectively) and the corresponding evolution of $T_{\rm b}$. Lower panel: Fit of the observational data (filled symbols) for XTE J1701−462 with a base cooling curve for $\dot{M}_{18} = 0.7 - 1.3$ and $T_{\rm c,8} = 1.3 - 1.8$: solid line minimizes χ^2 ($\chi^2 = 0.57$) and the brown region denotes curves with $\chi^2 < 1$. Dashed and dotted lines ($\chi^2 = 0.41, 0.37$) include residual accretion functions $\dot{M}_{A,B}(t)$, respectively.

fit without accretion after t_0; it predicts that the source is still cooling down. The dashed line is the temperature evolution including $\dot{M}_A(t)$ and fits the filled symbols plus CXO-2, XMM-1 and XMM2. The dotted line fits all the points including also XMM-3 and CXO-4 assuming the accretion rate $\dot{M}_B(t)$. Therefore, we need a mean accretion rate of about one third of the value of $\dot{M}$ during outburst to account for all observations.

Even though our results show that residual accretion can explain CXO-2, XMM-1 and XMM-2 observations, Fridriksson et al. (2011) stated that the thermal component outside flares (XMM-3 and CXO-4 observations) is unlikely to be due to ongoing low level accretion. This is because the evolution of temperature throughout quiescence (excluding flares) present an smooth and monotonic decrease; if accretion were a significant contribution to the thermal emission it would be observed much more irregular variability in this component. Moreover, there has not been

observed any correlation between thermal and non thermal fluxes outside flares, whereas both rise together during flares. Nevertheless the presence of residual accretion outside flares is a possibility that can not be conclusively ruled out.

11. Summary

We have presented detailed numerical models describing the thermal relaxation of the crust following long accretion periods, motivated by the increasing number of observations of MXB 1659−29, KS 1731−260, EXO 0748−676, XTE J1701−462 and IGR J17480−2446. Our main results are summarized as follows:

1. First, we check by fitting MXB 1659−29 observations that the energy released by pycnonuclear reactions ($\sim$0.05 MeV nuc^{-1}) does not seem to be enough to explain the high initial temperature ($\sim 10^8$ K). This confirms Brown & Cumming (2009) results, who estimated $\sim (0.7-0.8)$ MeV nuc^{-1} for MXB 1659−29 and KS 1731−260 (considering $\dot{M}_{18}=0.1$). Then, to explain cooling curves early slopes it its necessary to consider an additional inward-directed heat flux originated in outer layers.
2. We solve stationary thermal profiles for the envelope during the accretion stage. Considering different compositions we obtain $T_{\rm b}(\dot{M})$ relations that reduce the number of free parameters. In turn, as they depend on the envelope composition, we can set constraints on the hydrogen and helium fractions. Including these $T_{\rm b}(\dot{M})$ relations in our simulations, we fit successfully MXB 1659−29, KS 1731−260 and EXO 0748−676 observations.
3. We also study the influence of neutron superfluidity. MXB 1659−29 and EXO 0748−676 can be modeled with the same microphysics as in Brown & Cumming (2009). However, KS 1731−260 imposes an additional constraint on the neutron energy gap. The last observation suggests a longer relaxation time which is compatible with a smaller, deep gap with $\Delta \lesssim 0.1$ MeV at $\rho \lesssim 10^{13}$ g cm^{-1}. We did not find satisfactory solutions (with $\chi^2 \lesssim 1$) with the Sch03 gap for KS 1731−260, even varying the NS mass. On the other hand, MXB 1659−29 and EXO 0748−676 can be described by both gaps.
4. We conclude that MXB 1659−29, KS 1731−260 and EXO 0748−676 can be fit simultaneously with a canonical model which satisfy the following characteristics: the NS mass is rather low ($M = 1.4$ M$_\odot$), the impurity content is small ($Q_{\rm imp} \lesssim 5$) and the energy gap for neutron superfluidity has a small value ($\lesssim 0.1$ MeV) or it is peaked at relatively high density, deep in the inner crust ($\rho \sim 10^{14}$ g cm^{-3}). On the other hand, the favored envelope model is compound mostly of He ($X \lesssim 10\%$), and the appearance of heavy elements occurs at about $\rho_h \sim 3\times10^7$ (like PA$^{\rm deep}$).
5. There are two other sources, XTE J1701−462 and IGR J17480−2446 that present peculiar quiescent emission and require special attention. XTE J1701−462 can not be explained with a standard crustal cooling model. It requires additional heat sources located in the outer crust, at $\bar{\rho} \sim (0.5-8.0)\times10^{10}$ g cm^{-3}, releasing $q \sim (0.1-0.4)$ MeV nuc^{-1}. In addition, we explored alternative scenarios, as the presence of residual accretion during quiescence. Even though this model can explain data, the thermal component outside flares is unlikely to be due to ongoing low level accretion (Fridriksson et al. 2011). We also probe the scenario of the suppression of the electronic thermal conductivity in a thin layer due to a buried magnetic field. We found that the layer must be thin, ($\Delta r \sim (10-30)$ m) and located at $\rho \sim 10^{10}$ g cm^{-3}. For a better description it is necessary to solve a 2D problem considering the magnetic field geometry.
6. IGR J17480−2446 challenges our current understanding of crustal cooling since its thermal flux still remains above the value measured in the previous quiescent phase after spending 2.2 years in quiescence. This is difficult to reconcile with its short outburst (which lasted only two months). In agreement with Degenaar et al. (2013), we find that it is possible to explain the data if we consider that $T_{\rm c}$ is higher than the one measured in the last quiescent phase. Another possibility is, again, the presence of additional heat sources, but in this case they must be considerably more intense ($q \sim 3$ MeV nuc^{-1}) and must be located in a deeper layer ($\bar{\rho} \sim 10^{11}$ g cm^{-3}) than for XTE J1701−462.

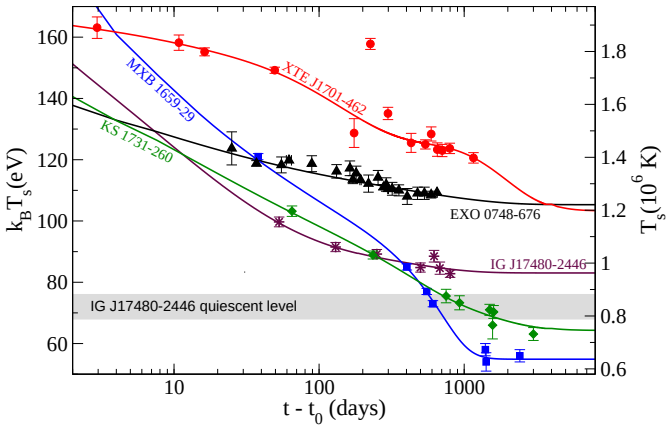

Fig. 26. Cooling curves comparison of all the sources. In each case we show the best fit corresponding to the models: crustal cooling (MXB 1659−29), crustal cooling with an small energy gap for neutron superfluidity (KS 1731−260), crustal cooling (all data fit, EXO 0748−676), crustal cooling with additional heat sources (XTE J1701−462) and crustal cooling with a high $T_{\rm c}$ (IGR J17480−2446).

In Fig. 26 we summarize our results, showing together the best fits obtained for all the sources. MXB 1659−29 and KS 1731−260 have already reached thermal equilibrium, with surface temperatures at $kT_{\rm eff} = 56.8$ eV and $kT_{\rm eff} = 64.3$ eV, respectively. EXO 0748−676 and IGR J17480−2446 seem also close to equilibrium levels, with temperatures of $kT_{\rm eff} = 105.3$ eV and $kT_{\rm eff} \sim 85.0$ eV, respectively. On the other hand, XTE J1701−462 is still far from thermal equilibrium, which will be reached in several years at the value $kT_{\rm eff} = 105$ eV. This high value is comparable to EXO 0748−676 while the other sources level off at much lower temperatures. XTE J1701−462 has an early observation, which provides valuable information about the position and intensity of heat sources in the outer crust.

Instead, we do not have information before ∼30 days for the other sources. An open question is if the other sources showed an early behavior similar to XTE J1701−462.

Acknowledgements. This research was partially supported by CONICET, PIP-2011-00170 (DNA) and by the grant AYA 2010-21097-C03-02 (JAP). DNA thanks Physics Dept. of Ohio University where part of this project started and Dept. of Applied Physics of Alicante University for warm hospitality.

Appendix A: Comparison with previous works

A.1. MXB 1659−29 results with BC09

In order to check our numerical approach and code we first compare our results for MXB 1659−29 with BC09 in which $\dot{M}$, $T_{\rm c}$, $T_{\rm b}$ and $Q_{\rm imp}$ are free parameters (Fig. A.1). Similarly as they did, we fix $M = 1.6$ M$_\odot$, $\dot{M}_{18} = 0.1$ and $Q_{\rm imp} = 4.0$ and explore the behavior of the cooling curves against the variation of $T_{\rm c}$ and $T_{\rm b}$. In Fig. A.1 the solid line corresponds to the best fit obtained with $T_{\rm c,8} = 0.29$ and $T_{\rm b,8} = 4.1$ ($\chi^2 = 0.54$). The brown zone is $\chi^2 < 2$ with parameters in ranges, $T_{\rm c,8} = (0.26 - 0.32)$ and $T_{\rm b,8} = (3.9 - 4.4)$.

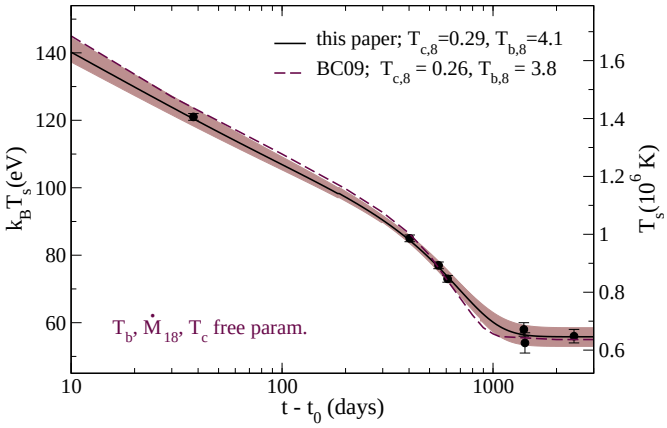

Fig. A.1. Comparison of our cooling curves for MXB 1659−29 with BC09. Solid line is our best fit with $\chi^2 = 0.54$ and the dashed line is BC09 result. The brown region are our curves with $\chi^2 < 2$ corresponding to $T_{\rm c,8} = 0.26 - 0.32$ and $T_{\rm b,8} = 3.9 - 4.4$. For all curves $\dot{M}_{18} = 0.1$ is fixed.

We found that observations can be well described by our cooling curves and they are in very good agreement with BC09 results (dashed line).

A.2. KS 1731−260 results with BC09 and Sht07

We compare in Fig. A.2 our cooling curves for KS 1731−260 with previous results of Sht07 (top panel) and BC09 (bottom panel). The dashed line in the top panel is taken from from Sht07 and the solid line is our result obtained by letting $T_{\rm b}$ to evolve freely (as in Sec. 6). We consider $\dot{M}$, $T_{\rm c}$ and $Q_{\rm imp}$ as free parameters, and find that data can be explained with the values $\dot{M}_{18} = 0.28$, $T_{\rm c,8} = 0.46$ and $Q_{\rm imp} = 2$, respectively. The NS mass is 1.6 M$_\odot$ and the neutron superfluidity energy gap in the crust is that of Wambach et al. (1993) (moderate superfluidity case in Sht07). For a better comparison of the results we show in addition to Cackett et al. (2010a) data (considered so far), observations from Cackett et al. (2006) (open circles) with 2σ error bars, which are the ones considered by Sht07.

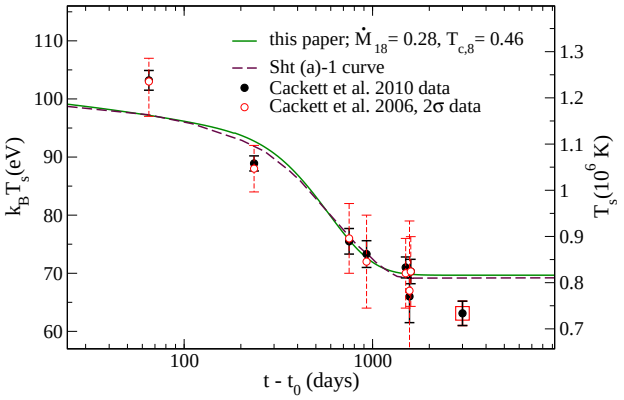

(a) Solid line is our curve with $Q_{\rm imp} = 2$. Dashed curve is from Sht07.

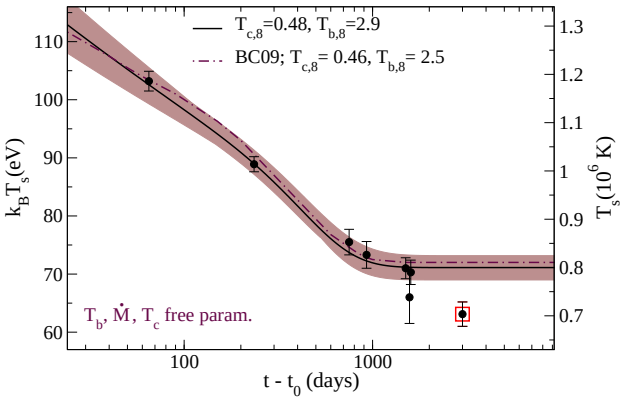

(b) Solid curve is our best fit with $\chi^2 = 0.5$. Fixed parameters are $\dot{M}_{18} = 0.1$ and $Q_{\rm imp} = 1.5$. Brown region corresponds to $\chi^2 < 2$ with free parameters varying in ranges, $T_{\rm c,8} = (0.45 - 0.51)$ and $T_{\rm b,8} = (2.5 - 3.4)$.

Fig. A.2. Comparison of our results for KS 1731−260 with Sht07 (upper panel) and BC09 (bottom panel). Solid curves are our fits and dashed and dotted dashed curves are Sht07 and BC09 results, respectively. $M = 1.6$ M$_\odot$ is fixed for all. The last observation (with a red square) was reported after the publication of those works.

In the bottom panel we compare our results with BC09, now $T_{\rm b}$ is fixed during outburst to a constant value (as in Sec. 6) and perform simulations were $T_{\rm c}$, $T_{\rm b}$ and $Q_{\rm imp}$ vary as free parameters. The doted-dashed line was taken from BC09 and the solid curve is our best fit with $\chi^2 = 0.5$. The brown region corresponds to $T_{\rm c,8} = (4.5 - 5.0)$ and

$T_{\rm b,8} = (2.5 - 3.2)$ with $\chi^2 < 2$; all these curves consider $Q_{\rm imp} = 1.5$ (the same value was used in BC09). The NS mass is fixed to 1.6 $M_\odot$ and we consider the Sch03 energy gap for neutron superfluidity in the crust.

We conclude that our curves are in good agreement with previous results, giving us confidence about our work.

References

Aguilera, D. N., Pons, J. A., & Miralles, J. A. 2008, A&A, 486, 255
Andersson, N., Comer, G. L., & Glampedakis, K. 2005, Nucl. Phys. A, 763, 212
Baym, G., Bethe, H. A., & Pethick, C. J. 1971, Nucl. Phys. A, 175, 225
Bildsten, L. 1997, arXiv:astro-ph/9709094
Bordas, P., Kuulkers, E., Alfonso-Garzón, J., et al. 2010, The Astronomer's Telegram, 2919, 1
Brown, E. F., Bildsten, L., & Rutledge, R. E. 1998, ApJ, 504, L95
Brown, E. F. & Cumming, A. 2009, ApJ, 698, 1020
Cackett, E. M., Brown, E. F., Cumming, A., et al. 2013, ApJ, 774, 131
Cackett, E. M., Brown, E. F., Cumming, A., et al. 2010a, ApJ, 722, L137
Cackett, E. M., Brown, E. F., Miller, J. M., & Wijnands, R. 2010b, ApJ, 720, 1325
Cackett, E. M., Wijnands, R., Linares, M., et al. 2006, MNRAS, 372, 479
Cackett, E. M., Wijnands, R., Miller, J. M., Brown, E. F., & Degenaar, N. 2008, ApJ, 687, L87
Campana, S., Colpi, M., Mereghetti, S., Stella, L., & Tavani, M. 1998, A&A Rev., 8, 279
Colpi, M., Geppert, U., Page, D., & Possenti, A. 2001, ApJ, 548, L175
Cooper, R. L. & Narayan, R. 2005, ApJ, 629, 422
Cumming, A., Macbeth, J., in 't Zand, J. J. M., & Page, D. 2006, ApJ, 646, 429
Degenaar, N., Brown, E. F., & Wijnands, R. 2011a, MNRAS, 418, L152
Degenaar, N. & Wijnands, R. 2011a, MNRAS, 414, L50
Degenaar, N. & Wijnands, R. 2011b, MNRAS, 412, L68
Degenaar, N. & Wijnands, R. 2012, MNRAS, 422, 581
Degenaar, N., Wijnands, R., Brown, E. F., et al. 2013, ApJ, 775, 48
Degenaar, N., Wijnands, R., Wolff, M. T., et al. 2009, MNRAS, 396, L26
Degenaar, N., Wolff, M. T., Ray, P. S., et al. 2011b, MNRAS, 412, 1409
Díaz Trigo, M., Boirin, L., Costantini, E., Méndez, M., & Parmar, A. 2011, A&A, 528, A150
Douchin, F. & Haensel, P. 2001, A&A, 380, 151
Fridriksson, J. K., Homan, J., Wijnands, R., et al. 2011, ApJ, 736, 162
Fridriksson, J. K., Homan, J., Wijnands, R., et al. 2010, ApJ, 714, 270
Galloway, D. K., Muno, M. P., Hartman, J. M., Psaltis, D., & Chakrabarty, D. 2008, ApJS, 179, 360
Gudmundsson, E. H., Pethick, C. J., & Epstein, R. I. 1983, ApJ, 272, 286
Gupta, S., Brown, E. F., Schatz, H., Möller, P., & Kratz, K. 2007, ApJ, 662, 1188
Haensel, P. & Zdunik, J. L. 2008, A&A, 480, 459
Heinke, C. O., Wijnands, R., Cohn, H. N., et al. 2006, ApJ, 651, 1098
Horowitz, C. J., Berry, D. K., & Brown, E. F. 2007, Phys. Rev. E, 75, 066101
Horowitz, C. J., Caballero, O. L., & Berry, D. K. 2009, Phys. Rev. E, 79, 026103
Horowitz, C. J., Dussan, H., & Berry, D. K. 2008, Phys. Rev. C, 77, 045807
in't Zand, J. J. M., Keek, L., Cumming, A., et al. 2009, A&A, 497, 469
Kaminker, A. D., Haensel, P., & Yakovlev, D. G. 2001, A&A, 373, L17
Levenfish, K. P. & Yakovlev, D. G. 1994, Astronomy Reports, 38, 247
Lewin, W. H. G., Hoffman, J. A., Doty, J., & Liller, W. 1976, IAU Circ., 2994, 1
Parmar, A. N., White, N. E., Giommi, P., & Gottwald, M. 1986, ApJ, 308, 199
Payne, D. J. B. & Melatos, A. 2004, MNRAS, 351, 569
Pooley, D., Homan, J., Heinke, C., et al. 2010, The Astronomer's Telegram, 2974, 1
Remillard, R. A., Lin, D., ASM Team at MIT, & NASA/GSFC. 2006, The Astronomer's Telegram, 696, 1
Rutledge, R. E., Bildsten, L., Brown, E. F., Pavlov, G. G., & Zavlin, V. E. 2000, ApJ, 529, 985
Rutledge, R. E., Bildsten, L., Brown, E. F., et al. 2002, ApJ, 580, 413
Schatz, H., Bildsten, L., Cumming, A., & Wiescher, M. 1999, ApJ, 524, 1014
Schulze, H. J., Baldo, M., Lombardo, U., Cugnon, J., & Lejeune, A. 1998, Phys. Rev. C, 57, 704
Schwenk, A., Friman, B., & Brown, G. E. 2003, Nucl. Phys. A, 713, 191
Shternin, P. S., Yakovlev, D. G., Haensel, P., & Potekhin, A. Y. 2007, MNRAS, 382, L43
Sunyaev, R. & Kwant Team. 1989, IAU Circ., 4839, 1
Wambach, J., Ainsworth, T. L., & Pines, D. 1993, Nucl. Phys. A, 555, 128
Wijnands, R., Miller, J. M., Markwardt, C., Lewin, W. H. G., & van der Klis, M. 2001, ApJ, 560, L159
Wijnands, R., Nowak, M., Miller, J. M., et al. 2003, ApJ, 594, 952
Wolff, M., Ray, P., Wood, K., & Wijnands, R. 2008, The Astronomer's Telegram, 1812, 1
Yakovlev, D. G., Kaminker, A. D., Gnedin, O. Y., & Haensel, P. 2001, Phys. Rep., 354, 1